Fall 2017

A Correlational Study of SansEC Sensors' Electric Field Distribution on Lightning Attachment

Kayla M. Farrow
Old Dominion University

A CORRELATIONAL STUDY OF SANSEC SENSORS' ELECTRIC FIELD DISTRIBUTION ON LIGHTNING ATTACHMENT

by

Kayla M. Farrow
B.S. May 2015, Old Dominion University

A Thesis Submitted to the Faculty of
Old Dominion University in Partial Fulfillment of the
Requirements for the Degree of

MASTER OF SCIENCE

ELECTRICAL AND COMPUTER ENGINEERING

OLD DOMINION UNIVERSITY
December 2017

Approved by:

Linda Vahala (Director)

Dean Krusienski (Member)

Julie Hao (Member)

ABSTRACT

A CORRELATIONAL STUDY OF SANSEC SENSORS' ELECTRIC FIELD DISTRIBUTION ON LIGHTNING ATTACHMENT

Kayla M. Farrow
Old Dominion University, 2017
Director: Dr. Linda Vahala

Old Dominion University and the National Aeronautics and Space Administration (NASA) Langley Research Center (LaRC) Aviation Safety Program Atmospheric Environmental Safety Technologies Project team conducted research in using SansEC (Sans Electric Connection) sensors to provide lightning strike protection (LSP) and damage mitigation for composite aircraft. SansEC sensors are simplistic devices consisting of an open circuit conductive trace, shaped in a planar geometric spiral [1], [2], [3]. SansEC sensors can be designed in various shapes and sizes depending on the application. For applications on exterior aircraft surfaces, the sensor must be designed to perform the required lightning strike protection [1], [3].

Lightning-direct effect current tests were conducted on multiple sensor configurations to evaluate their ability to withstand the incident lightning energy and protect the underlying composite [3]. Test results indicated several SansEC sensor geometric configurations demonstrated an intrinsic ability to steer the lightning current along the corner of the sensor [3]. This was a significant finding because when lightning strikes an airplane, its current is channeled onto the aircraft surface at an attachment point and flows along the aircraft surface to the detachment point and can cause damage to critical points on the aircraft that can be catastrophic [3], [4], [5]. The SansEC sensors' intrinsic ability to steer lightning current could be used to deflect lightning current from an

attachment or detachment point to a less critical point on an in-flight aircraft, to mitigate detrimental damage.

To investigate this phenomenology, electromagnetic computational simulations were conducted to calculate the electric field distribution on the SansEC sensors' conductive trace to determine if the associated electromagnetic radiation preceding lightning attachment establishes modal structures on the conductive trace which predisposition the direction of the current flow [3]. The simulations provided a means to visualize the trace's modal structure and identified electric field regions residing on the sensor [3]. This thesis presents a correlational study of the SansEC sensors' computed electric field distribution to the measured lightning propagation direction for various SansEC sensor configurations [3].

This thesis is dedicated to my exceptional significant other, Andy, and my outstanding family and friends for their encouragement, support, and patience.

ACKNOWLEDGMENTS

There are numerous individuals who have contributed to the successful completion of this thesis. I extend many thanks to my advisor and committee chair, Dr. Linda Vahala and to my thesis committee members, Dr. Dean Krusienski and Dr. Julie Hao, for their continued guidance, patience, and support of my research as a master's student.

I am truly grateful to have had the opportunity to work alongside world-class researchers at the National Aeronautics and Space Administration (NASA) Langley Research Center (LaRC) Electromagnetic and Sensors Branch in Hampton, Virginia. I extend many thanks to NASA Langley LaRC researchers George Szatkowski, Kenneth Dudley, and Laura Smith for their encouragement, guidance, patience, and support.

I extend many thanks to Dr. C.J. Reddy and the engineers and staff at Altair Engineering Inc (formerly EM Software & Systems), in Hampton, Virginia, for the generous providing of FEKO software and technical support.

I previously presented portions of this research at the International Conference on Lightning and Static Electricity (ICOLSE) on September 2013.

This work was partially funded by the Virginia Space Grant Consortium (VSGC) and the National Institute of Aerospace (NIA).

NOMENCLATURE

a	Wire Radius
A	Ampere
B	Magnetic Flux Density
C	Capacitance
dB	Decibels
E	Electric Field
ε_0	Free Space Permittivity
ε_r	Relative Permittivity
f	Frequency
H	Magnetic Field
hr	Hour
Hz	Hertz
I	Current/Current Amplitude
in	Inch
j	Imaginary Unit/Number
J	Current Density
l	Length of Sensor Trace
L	Inductance
ln	Natural Logarithm
m	Meter
$mils$	Thousandth of an Inch
min	Minute
N	Number of Turns

R	Resistance
sec	Second
S11	Reflection Coefficient
t	Time
$Tan\delta$	Loss Tangent
v	Velocity
V	Voltage
Z	Impedance
μ_0	Free Space Permeability
μ_r	Relative permeability
π	Pi
ρ	Charge Density
σ	Standard Deviation
φ	Magnetic Flux
ω	Angular Frequency
Ω	Ohms

TABLE OF CONTENTS

Page

LIST OF TABLES

LIST OF FIGURES

Figure Page

Page

CHAPTER I

INTRODUCTION

A. PURPOSE

The National Aerospace Research Center estimates that lightning strikes an aircraft on average every 1,000 flight hours [4]. For commercial airlines, this is the equivalent of one strike per aircraft per year [4]. While an aircraft is in use, it remains very challenging to predict or indicate the amount or intensity of impairment or inchoate fault due to lightning [4], [5]. The effects of lightning attachment are still causes of major concern to the aerospace industry today, where the consequences of such an event, in the absence of an adequate lightning strike protection (LSP) design, can be catastrophic.

Table 1 lists several catastrophic aircraft crashes that were influenced by lightning [4], [6], [7-11]. These events triggered the improvement of lightning protection standards for aircraft [12].

TABLE 1. AIRCRAFT CRASHES INFLUENCED BY LIGHTNING

Year	Location of Crash	Aircraft	Flight	Casualties	Survivors
1959	Marnate, Italy	Lockheed Starliner	TWA Flight 891	68	None
1963	Elkton, Maryland	Boeing 707	Pan Am Flight 214	81	None
1971	Puerto Inca, Peru	Lockheed L-188A Electra	LANSA Flight 508	91	1
1988	Kettwig, Germany	Metro III	Nürnberger Flugdienst Flight 108	21	None
2000	Hubei, China	Xian Y-7	Wuhan Airlines Flight 343	49	None

Coincidentally, fatal crashes due to lightning occurred after the 1950s and during the 1960s, as the aerospace industry began a major transition in airframes material structure, from aluminum to non-conductive composites such as carbon fiber and fiberglass [13]. This transition was due to the strength, flexibility, lightweight, and low cost of composite material in comparison to metal materials [13]. There has been substantial research performed to understand these composites' unique structural and mechanical properties, enabling their widespread use in the aerospace industry [13]. However, the demand for using composite materials in an aeronautic design has resulted in an increase in complexity of effects of a lightning strike, and the behavior of these composites in lightning environments causes major concern for the aerospace industry. The demand has led to new challenges in aircraft protection and has created an urgent need for improved understanding and elevated standard levels. The increased use of composite materials on aircraft increased the risk for probable damage and failure of composite aircraft structures due to lightning effects. When lightning strikes an airplane, the lightning current is channeled onto the aircraft surface at an attachment point and flows along the aircraft surface to the detachment point and can potentially cause damage [5]. New technologies in this area should be further investigated for the improvement of lightning protection standards.

B. PROBLEM

Old Dominion University and the National Aeronautics and Space Administration (NASA) Langley Research Center (LaRC) Aviation Safety Program Atmospheric Environmental Safety Technologies Project team conducted research to develop a multifunctional sensor technology to provide both lightning strike protection (LSP) and

damage detection for composite airframes [1]. These sensors are known as Sans Electrical Connection (EC) and an illustration of one is shown in Fig. 1.

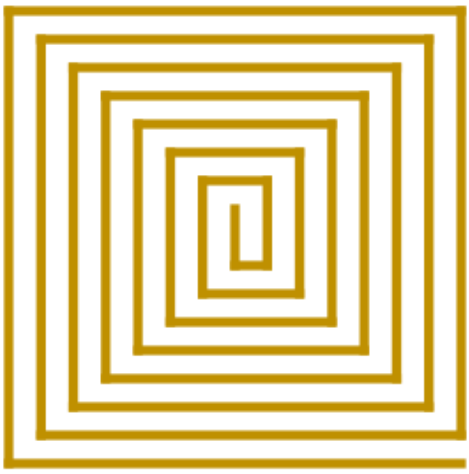

Fig. 1. Illustration of a SansEC Sensor

A SansEC sensor is an open-circuit resonator composed of a single self-resonant coil made of conductive material usually in a planar spiral pattern or helix structure [2], [14]. The sensor has inherent inductance, resistance, and capacitance based on its geometric design and is a passive device, meaning it does not supply power [1], [2], [14].

Lightning-direct current effect tests were conducted on numerous sensor configurations. Each configuration was initially evaluated on fiberglass panels to develop an understanding of how the sensors' geometry influenced lightning attachment and propagation on a dielectric substrate [4]. The SansEC lightning test articles were housed in a lightning testbed during test current attachment to monitor the current propagation off the four sides of the test panel to determine the propagation direction of the electric current.

The testbed was also instrumented with an infrared (IR) camera to measure the backside temperatures during the lightning strike. The sensors' conductive traces and ground paths generate resistive heating from the lightning current and temperature imagery allows visualization of lightning attachment and current propagation.

Several sensor configurations demonstrated an intrinsic ability to propagate the lightning current along one corner of the sensor, in effect, steering the lightning currents [3]. This was a significant finding because when a lightning strikes an aircraft, its current is channeled onto the aircraft surface at an attachment point and flows along the aircraft surface to a detachment point and can cause damage to critical points on the aircraft that can be catastrophic [5]. The sensors' intrinsic ability to steer lightning current could be used to deflect lightning current from an attachment or detachment point to a less critical point on an in-flight aircraft.

To investigate this phenomenon further, computational simulations were developed to explore the characteristic electric and magnetic field structures on the sensors' trace at their primary resonance frequency for these configurations [3]. The frequency content of a lightning waveform falls within the operational frequency resonance bands for the sensor configurations that were tested [3], [14]. As the lightning arc propagated toward the test panel its radiated electromagnetic field generated a self-resonance on the sensors, establishing electric and magnetic field modal structures on the sensors' spiral trace [3], [14]. Computational simulations were performed to visualize the electric and magnetic field structures residing on the sensors' trace [3]. The visualization data of the electric and magnetic field structures were then compared to the IR images to correlate high electric and magnetic field strength with lightning attachment and propagation [3].

CHAPTER II

LITERATURE REVIEW

This section presents the applicable laws, principals, and theories of the SansEC sensor technology framework. To understand the basis of the sensor technology, it is first important to understand the mathematical models and fundamentals of circuit and electromagnetic theory.

A. CIRCUIT THEORY

SansEC Sensor Circuit:

The sensor is a circuit with inherent inductance, resistance, and capacitance based on its geometric design [1], [2]. A circuit schematic of a SansEC sensor is shown in Fig. 2,

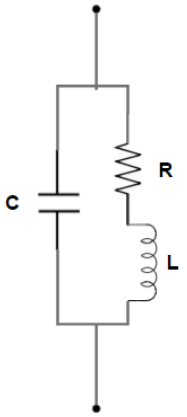

Fig. 2. Schematic representation of SansEC sensor

where L is the inductance, R is resistance, and C is the capacitance [14], [15]. Capacitance is the ability to store an energy in an electrical field [16], [17]. Resistance the measure of a material's capacity to impede that flow of elections [16], [17]. Inductance is the ability to store energy in a magnetic field [16], [17].

The sensors' capacitance is expressed in (1),

$$C = (\frac{1}{2\pi f\sqrt{L}})^2 \tag{1}$$

where f is the resonant frequency in hertz (Hz), L is the inductance measured in henrys (H), and C is the capacitance measured in farads (F) [14], [15]. The sensors' capacitance is due to the gaps of separation between the spiral traces and adjacent turns and dielectric substrate the sensor is placed on and the environment the sensor is in [1], [2].

The sensors' inductance is the sum of the mutual individual traces and their interactions when electromagnetically excited, the impedance from the ohmic loss along the conductive trace of the sensor, and the loss in the dielectric substrate the sensor is placed on or the environment the sensor is in. An approximation of the inductance of a square SansEC sensor is provided by Missouri Electromagnetic Compatibility Laboratory in (2),

$$L = N^2 \frac{2\mu_0\mu_r w}{\pi}[\ln(\frac{w}{\alpha}) - 0.774] \tag{2}$$

where L is the inductance, N is the number of turns, μ_0 is the permeability of free space, μ_r is the relative permeability of the material the sensor is made of, w is the length of one side of the sensor in centimeters (cm), and α is the wire radius in cm [14].

There are two components to the resistance of the sensor, represented as R in the schematic, the parallel and series resistance. The parallel resistance is the resistance between the sensor and a substrate [2], [14]. The series resistance is composed of two components, one dependent and one independent on frequency [2], [14]. The series resistance that is dependent on frequency is caused by currents effects [2], [14]. The series resistance that is independent of frequency is the direct current resistance of the conductive

trace of the sensor, which varies depending on the thickness and length of the conductive trace [2], [14].

The sensors' operational frequency correlates to the resonant frequency of the sensor [2], [9]. Resonant frequencies are frequencies at which a response amplitude is a relative maximum and is determined by the capacitance and inductance of the sensor [14], [15]. The resonant frequency of the sensor is inversely proportional to the square root of C and L [14], [15]. The inversely proportional relationship implies that when the capacitance and/or inductance decreases, the resonant frequency increases. This is expressed in (3),

$$f = \frac{1}{2\pi\sqrt{LC}} \tag{3}$$

where f is the frequency in Hz, L is the inductance, and C is the capacitance [14], [16]. The operational bandwidth of the sensors' resonant response includes the primary and harmonic resonance(s) which are dependent upon both the sensor's geometry and substrate in the proximity of the sensor [1], [2], [14].

Ohm's Law:

The SansEC sensor is a circuit and the basics of any circuit begin with Ohm's Law [14]. At the circuit level, current is a measure of the flow of electrons, resistance is the measure of a material's capacity to impede that flow of elections, and voltage is the electrical potential energy between two points in a circuit [16]. Ohm's Law expresses the relationship between current, voltage, and resistance in a circuit. Ohm's Law states that the current between two points in a circuit is a function of the voltage across those two points [16]. One representation of Ohm's Law is expressed in (4),

$$I = \frac{V}{R} \tag{4}$$

where I is the current measured in amperes (A), V is the voltage measured in volts (V), and R is the resistance measured in ohms (Ω) [16], [17]. From (4) it is apparent that current is not only directly proportional to voltage but inversely proportional to the resistance [16]. (4) is the Ohm's Law expression for direct current (DC). Ohm's Law also applies to alternating current (AC) as expressed in (5),

$$I = \frac{V}{Z} \tag{5}$$

where I and V are current and voltage, respectively and Z is impedance measured in ohms [16]. Impedance is the extension of resistance to AC circuits, having amplitude and phase components. There are two components to impedance real and imaginary [16], [17]. The real component is known as the resistive impedance (same resistance represented in a DC circuit) [17]. Ideal resistors are purely real [17]. The real component represents energy as heat dissipated [17]. Ideal capacitors and inductors are purely imaginary [16], [17]. The imaginary component is known as the reactive impedance [16], [17]. The total impedance is represented in (6),

$$Z = R + jX \tag{6}$$

where R is the resistance, X is the reactance, and j is the imaginary unit [16], [17]. The total reactance, X, is composed of two components inductance reactance and capacitance reactance as expressed in (7),

$$X = X_L + X_C = \omega L - \frac{1}{\omega C} \tag{7}$$

where C is capacitance, L is inductance, and ω is angular frequency (and $\omega = 2\pi f$) [16], [17].

The resistance is responsible for the energy dissipation as heat in a circuit and the reactance is responsible for the energy stored in a circuit and later returned [17]. Specifically, an inductor stores energy in a magnetic field and a capacitor stores energy in an electric field and later returns the energy to the circuit as voltage and current, respectively [16].

Kirchhoff's Law:

Kirchhoff's Current Law (KCL) defines the principle of conservation of electrical charge and implies that at any node in a circuit, the sum of currents flowing into to the node is the same as the sum of the currents flowing out of the node [14], [18]. KCL is represented by (8),

$$\sum_{k=1}^{n} I_k = 0 \tag{8}$$

where n is the total number paths with current flowing either toward or away from the node [14], [18].

Similarly, Kirchhoff's Voltage Law (KVL) defines the principle of conservation of energy and implies that the sum of the voltage or electrical potential difference around a closed circuit is zero [14], [19]. KVL is represented by (9),

$$\sum_{k=1}^{n} V_k = 0 \tag{9}$$

where n is the total number of voltages measured between two or more nodes [14], [19].

The sensors are intrinsically open circuits and thus have no current flow; meaning that KCL currents and KVL voltages are zero [14], [18], [19]. KCL is only applicable if current passes into one end of a conductor and passes out of the other end [18]. This is also

the case at DC or at low frequencies; however, at high frequencies, KCL and KVL apply to the sensors due to the parasitic capacitance distributed across the conductive trace of the sensor [14], [19]. Parasitic capacitance is the unintended capacitance, due to relative proximity, that exists between different parts and/or components in a circuit [14], [20]. The sensors' parasitic capacitance is a result of the geometry and the gap of separation between the adjacent turns of the spiral conductors [1], [14]. The gaps between the traces of the sensor form a capacitance region where charge can flow; hence, creates a closed resonant circuit and increases the inductive component [1], [2], [14].

B. ELECTROMAGNETIC THEORY

Biot–Savart Law & Ampère's Law:

The Biot-Savart Law describes the magnetic field and intensity at a position in a wire conductor generated by an electric current [21]. It relates the direction, length, magnitude, and proximity of the electric field to the magnetic field [21], [22]. The magnetic field's intensity is directly proportional to the current and inversely proportional to the distance between the location on the conductor and where the magnetic field is calculated [21]. This is expressed in (10),

$$\mathbf{H}(\mathbf{r}) = \frac{\mu_0}{4\pi} \int_C \frac{I d\mathbf{l} \times \hat{\mathbf{r}}'}{|\mathbf{r}'|^2} \tag{10}$$

where this equation computes the resultant magnetic field **H**, and d**l** is the vector line representing length of the conductor carrying electric current I, **r** is the distance between the location on the conductor (d**l**) and where the magnetic field is being calculated, $\hat{\mathbf{r}}$ is a unit vector in the direction of **r**, all integrated over a path C, and μ_0 is the permeability, the measure of a substance's ability to form a magnetic field [14], [21], [22]

A circuit's magnetic field can be simplified from Biot-Savart Law using Ampère's Law is expressed in (11),

$$\oint \mathbf{H} d\mathbf{l} = \mu I \tag{11}$$

where the line integral is over an arbitrary loop, **H** is the magnetic field, I is the current enclosed by the loop, and μ_0 is the permeability [14], [23], [24]. Ampère's Law relates magnetic fields to electric currents and conversely, by determining either current associated with magnetic fields or magnetic field associated with a current with the constraint of that electric field does not change with time [23], [24].

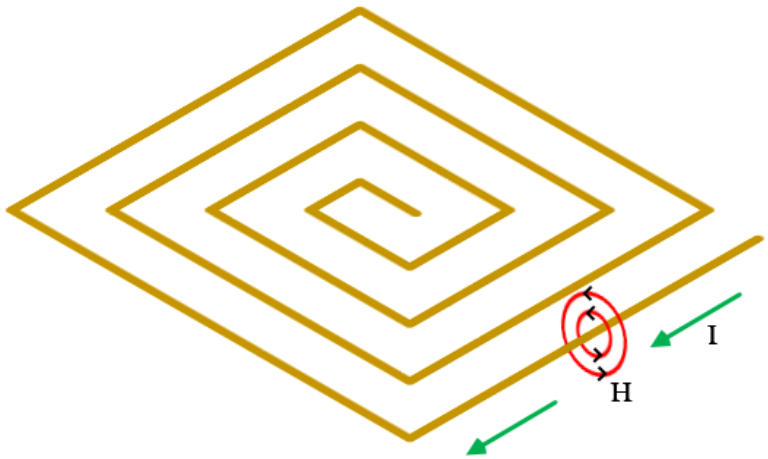

Fig. 3. Illustration of Ampère's Law applied to a SansEC sensor*

* Figure 3 was adapted from Figure 5.2 of [14].

Figure 3 illustrates Ampère's Law on a SansEC sensor [14]. The illustration depicts a directional current I along the SansEC trace using a green arrow and a directional magnetic field H around the sensor's trace using a red arrow [14], [23], [24].

If time-varying electric fields are present on the sensor, Ampère's Law alone no longer applies and the extensions to Ampère's Law, Maxwell's equations, must be used to describe the relationship between electricity and magnetism [14], [24].

Faraday and Lenz's Law:

Faraday's Law describes a phenomenon called electromagnetic induction – the interaction of a magnetic field with an electrical circuit to produce an electromotive force (EMF) or voltage [25]. As a changing magnetic field moves through a spiral, coil, or loop in a circuit, it generates an electric force which drives the current through that spiral, coil, or loop [14], [25]. Faraday's Law is expressed in (12),

$$\xi = -\frac{\mathrm{d}\phi_H}{\mathrm{d}t} \tag{12}$$

where Ɛ is the EMF, dt is the time rate of change, and φ_H is magnetic flux [14], [25], [26]. The surface integral of the normal component of a magnetic field that passes through that surface is the magnetic flux [26]. Lenz's Law is described in the EMF equation by the negative sign associated with the change of magnetic flux over time, because a current that is created by a changing magnetic field (in a coil, loop, or spiral) creates an opposing magnetic field in the magnetic field that induced it [14], [27].

A spiral or coil in a circuit that is tightly wounded with N number of identical turns, all with the same magnetic flux, is expressed in (13),

$$\xi = -N\frac{\mathrm{d}\phi_H}{\mathrm{d}t} \tag{13}$$

where φ_H is the magnetic flux through a single loop [14], [25], [26].

The formulations of Faraday and Lenz's law of induction varies for different geometries of inductive coils and spirals and applies to SansEC because of its planar spiral geometry [25].

Maxwell's Equations:

Maxwell's first equation is Gauss's Law for electricity which states that electric charge acts as either a source or sink for an electric field meaning that the divergence of the vector field is either positive or negative, respectively [28], [29]. This relates an enclosed electric charge to the electric flux through any closed Gaussian surface [28], [29]. Gauss's Law for electricity is expressed in (14) as the divergence of the electric field equal to the electric charge density divided by the intrinsic electric permittivity of free space,

$$\nabla \cdot \mathbf{E} = \frac{\rho}{\epsilon} \tag{14}$$

where the divergence of the electric field is $\nabla \cdot \mathbf{E}$, ρ is the electric charge density, and ε is the electric permittivity [14], [28], [29]. Divergence is defined as the volume density of an outward flux of a vector field around a point [25].

The sensors' electric charge distribution is given in (14); however, if the sensor is placed on a substrate then the charge due to the polarization of the substrate would be included in the equation by changing the permittivity [2], [14], [28], [29].

Maxwell's second equation is Gauss's Law for magnetism which states that the net magnetic flux out of any closed surface is zero [28], [29]. Gauss's Law for magnetism is expressed in (15) as the divergence of the magnetic flux equal to 0,

$$\nabla \cdot \mathbf{H} = 0 \tag{15}$$

where the divergence of the magnetic flux is $\nabla \cdot \mathbf{H}$ [14], [28], [29]. It is important to note that the net magnetic flux through a closed surface is zero [28], [29].

The sensors produce magnetic fields that are described as dipoles that resemble positive and negative magnetic charges comparable to electric charges, though inseparable [2], [14], [28], [29]. Fig. 4 shows an illustration of the current flowing on a SansEC sensor traces and the magnetic field lines that the current generates [14].

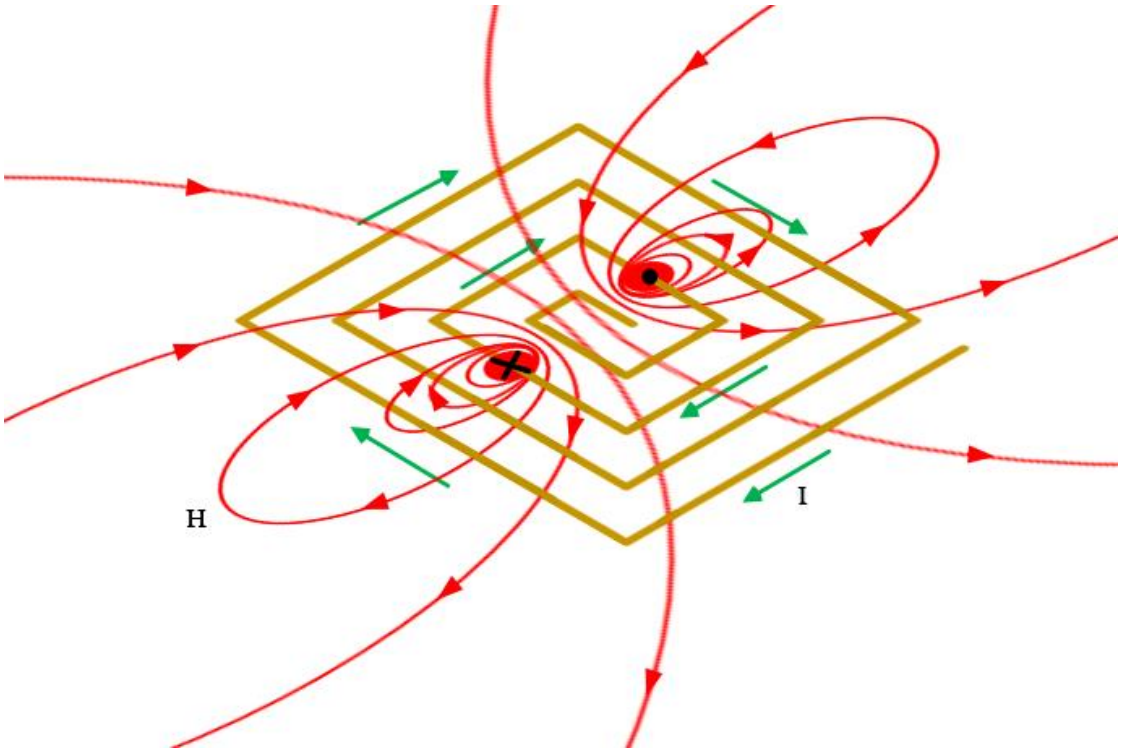

Fig. 4. Magnetic field due to current flow in a SansEC at resonance*

* Figure 4 was adapted from Figure 5.4 of [14].

Maxwell's third equation is an extension to Ampère's Law stating that a changing magnetic field induces an electric field and similarly, a changing electric field induces a magnetic field and is expressed in (16),

$$\nabla \times \mathbf{H} = -\epsilon \frac{\partial \mathbf{E}}{\partial t} + \sigma \mathbf{E} \tag{16}$$

where curl of the magnetic field ∇ x **H**, **E** is the electric field, Ɛ is the electric permittivity σ is the electric conductivity, and t is time [14], [28], [29]. The curl is the circulation around a given point [30]. The magnetic field around the closed loop is directly proportional to the electric current summed with the rate of change of the electric field the loop encloses [28], [29].

Maxwell's fourth equation is an extension of Faraday's Law of induction stating that a time-varying magnetic field induces an electric field and is expressed in (17),

$$\nabla \times \mathbf{E} = -\mu \frac{\partial \mathbf{H}}{\partial t} \tag{17}$$

where the curl of the electric field ∇ x **E, H** is the magnetic field, and t is time [14], [28], [29]. The induced voltage in a closed loop is directly proportional to the rate of change of the magnetic flux the loop encloses [28], [29].

This extension of Faraday's Law in Maxwell's equation is an essential principle in applying antenna interrogation to a SansEC sensor [14], [25]. During this interrogation, a loop antenna couples a changing magnetic field to the sensor which induces an electric field that is coupled to the substrate near the sensor [2], [14], [31]. This interrogation system is further discussed in more detail in the Antenna Theory section in II. C.

C. ANTENNA THEORY

The antenna interrogation system in this study has four components: a network analyzer, a near-field loop antenna, a SansEC sensor, and the substrate that the sensor is on [2], [14], [31]. An illustration of this system is shown in Fig. 5.

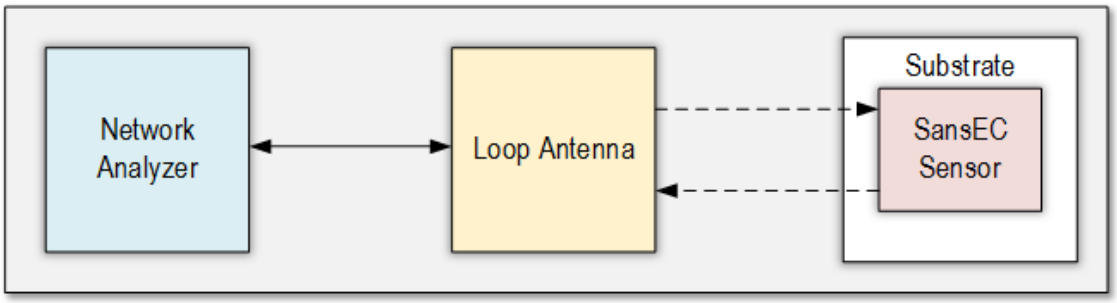

Fig. 5. Antenna Interrogation System

The network analyzer and loop antenna are connected via a coax cable. The network analyzer generates electromagnetic signal of a specified voltage, frequency, magnitude, and phase [31], [32]. The loop antenna transmits a broadband continuous electromagnetic wave from the network analyzer which triggers the sensors' self-resonance, passively [2], [14], [31], [33]. The loop antenna then receives a frequency response from the sensor [2], [14], [31], [33]. The sensors' resonant response is influenced by the electric impedance of the substrate within the boundary of its resonating near-field. The electric impedance of the substrate is reflected in the sensors resonant response and enables it to detect permittivity, permeability, and conductivity changes [2], [14], [31], [33].

The antenna interrogation system can be represented as an impedance model as shown in Fig. 6 [14].

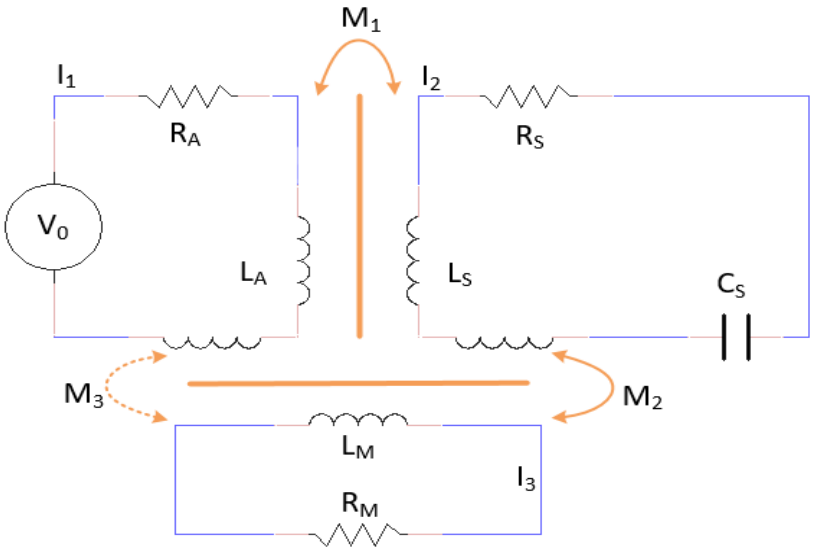

Fig. 6. Circuit model of a loop antenna, SansEC sensor, and substrate*

The impedance of the near-field loop antenna is expressed in (21),

$$Z_A = R_A + j\omega L_A \tag{21}$$

where Z_A is the total impedance, R_A is the resistive impedance, and L_A is the inductive reactance, j is the imaginary unit, and ω is angular frequency [1], [14], [16], [17].

The impedance of the sensor is expressed in (22),

* Figure 6 was adapted from Figure 5.6 of [14].

$$Z_S = R_S + j(\omega L_S - \frac{1}{\omega C_S}) \tag{22}$$

where Z_S is the total impedance, R_S is the resistive impedance, L_S is the inductive reactance, C_S is the capacitive reactance, j is the imaginary unit, and ω is angular frequency [1], [14], [17].

The impedance of the dielectric substrate is expressed in (23),

$$Z_M = R_M + j\omega L_M \tag{23}$$

where Z_M is the total impedance, R_M is the resistive impedance, L_M is the inductive reactance, j is the imaginary unit, and ω is angular frequency [1], [14], [16], [17].

KVL can be used on the circuit model to solve a system of equations in (24),

$$\begin{bmatrix} Z_A & j\omega M_1 & j\omega M_3 \\ j\omega M_1 & Z_s & j\omega M_2 \\ j\omega M_3 & j\omega M_2 & Z_M \end{bmatrix} \begin{bmatrix} I_1 \\ I_2 \\ I_3 \end{bmatrix} = \begin{bmatrix} V_{source} \\ 0 \\ 0 \end{bmatrix} \tag{24}$$

where I_1 is the current of the antenna circuit, I_2 is the current of the sensor, I_3 is the current of the dielectric substrate, M_1 is the mutual inductance between the sensor and the antenna, M_2 is the mutual inductance between the sensor and the dielectric substrate, M_3 is the mutual inductance between the antenna and the dielectric substrate, and V_{source} is the voltage source [14], [16], [17], [33]. The total impedance of the circuit is calculated using Ohm's Law and is expressed in (25) [14], [16], [17].

$$Z_{load} = \frac{V_{source}}{I_1} \tag{25}$$

The impedance model that is shown in Fig. 6 is simplified to a single circuit model in Fig. 7. Fig. 7 illustrates a simplified one-port impedance circuit, where Z_{load} is the

impedance towards the load and Z_{source} is the impedance towards the voltage source [14], [33], [34].

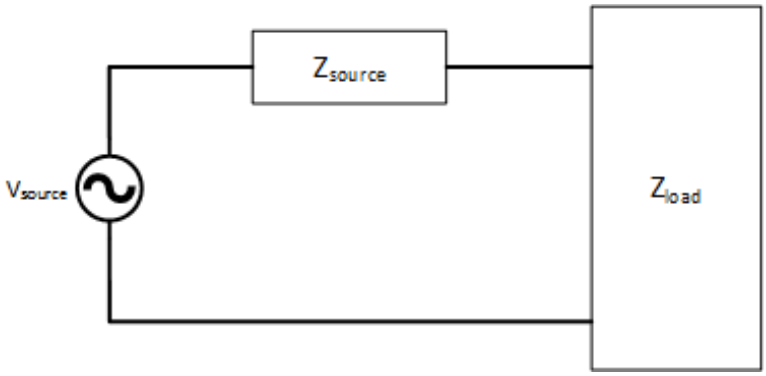

Fig. 7. Simplified one-port impedance circuit

The reflection coefficient (return loss one-port S parameter, S11) is a parameter describing how much power is reflected or returned back to source over the amount that is delivered to the SansEC (the load) and is expressed in (26) as a ratio of difference between the load and source impedance and the sum of the load and source impedance [33], [34]. In other words, it describes how much power is and is not absorbed by the SansEC (load).

$$S_{11} = \frac{Z_{load} - Z_{source}}{Z_{load} + Z_{source}} \tag{26}$$

The reflection coefficient in this study is plotted against frequency. The primary resonant frequency of a SansEC sensor is determined by the minimum amplitude of the reflection coefficient, where the power absorption of the sensor is at its maximum value [14], [33], [34], [35]. Fig. 8 shows a simulated frequency response plot of a SansEC sensor as reflection coefficient versus frequency.

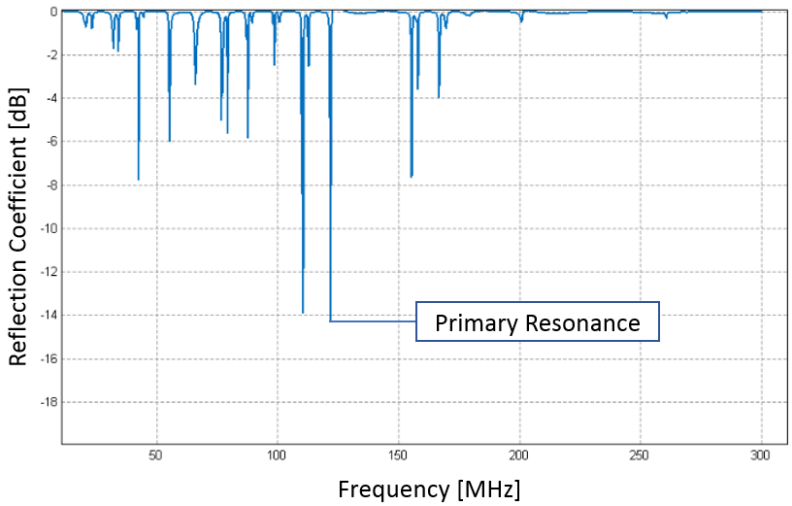

Fig. 8. Simulated frequency response plot of a SansEC sensor

It is important to note that in this study the antenna interrogation system is simulated using electromagnetic simulation software. The details of this are discussed in the Methodology Section III.B.

In this literature review, the laws, fundamentals, and principles of circuit, electromagnetic, and antenna theory were presented to build the foundation, theoretical context, and conceptual basis of the SansEC sensor technology framework.

CHAPTER III

METHODOLOGY*

A. LIGHTNING TESTS

1) Lightning Test Facility

The lightning tests were conducted at the National Technical Systems' (NTS) Lightning Technologies (LTI) facility in Pittsfield, Massachusetts in February 2012 [36].

2) SansEC LSP Test Panel

The SansEC lightning LSP configuration articles were composed of 1.25 mil thick copper tape that encompassed the edges of the panel, the ground paths, and the SansEC sensor [3]. The sensors were of a square geometry of 7x7 inches, 8x8 inches, and 9x9 inches. The sensors' conductive trace width was 93.75 mils and the gap width was 31.25 mils. The endpoint of the sensor spiral trace was always positioned at the lower right corner of the panel, with the trace proceeding in a clockwise manner to the center. The SansEC LSP configurations articles were bonded on fiberglass reinforced polymer (FRP) panels that were approximately 0.25-inch thick and 20x20 inches square. The surface of the panel was coated with a dielectric aerospace paint and primer, approximately 6 mils thick. The SansEC LSP test panel parameters are shown in Table 2.

* Portions of this research were previously presented at the International Conference on Lightning and Static Electricity (ICOLSE) 2013 in Seattle, Washington [3].

TABLE 2. PARAMETERS OF SANSEC LSP TEST PANELS

SansEC Parameters	7-inch	8-inch	9-inch
Trace Width	93.75 mils		
Trace Gap Width	31.25 mils		
Material Thickness	1.25 mils		
Dimensions	7 in. x 7 in.	8 in. x 8 in.	9 in. x 9 in.
Ground Paths Parameters			
Material Thickness	1.25 mils		
Dimensions (4 inner)	2 in. x 15 in.		
Dimensions (4 outer)	1 in. x 18 in.		
FRP Parameters			
Material Thickness	0.25 in.		
Dimensions	20 in. x 20 in.		
Dielectric Paint (and Primer) Parameters			
Material Thickness (Primer)	1-3 mils		
Material Thickness (Paint)	4-6 mils		
Dimension Coverage	20 in. x 20 in.		

Fig. 9 shows a photograph of a lightning test panel with a 7-inch SansEC LSP panel and the ground path surrounding it before the paint was applied.

Fig. 9. Actual Test Panel with 7-inch SansEC (shown unpainted) [3], [14]

3) Lightning Test Setup

The panels were mounted in a testbed prior to the lightning test. The panels were then tested with a peak current of 40 kiloamperes (kA). To determine the propagation direction of the electric current, four Pearson 4418 current probes were used to monitor the electric ground current off the edges of the test panel [37]. The current probes were connected to an oscilloscope via a 50 Ω output cable [37].

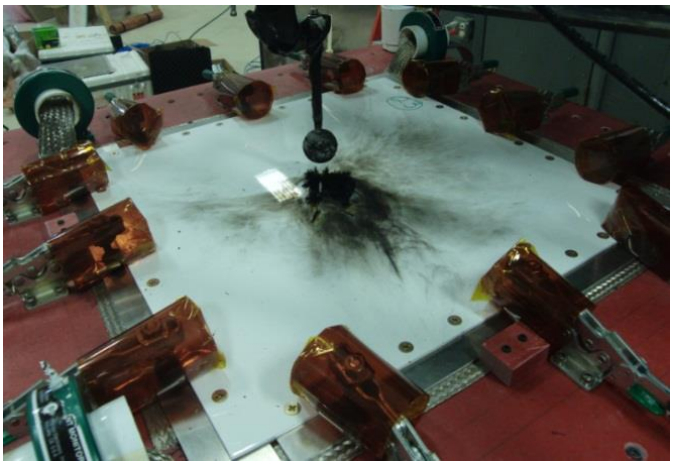

Fig. 10. Photograph of carbon fiber test panel installed in testbed at LTI [3], [14]

The lightning electrode was positioned at the center of each test panel, right above the SansEC sensor, for each test. Fig. 10 shows a photograph of the test panel installed at the testbed. Pearson probe current monitors are visible in the picture at the corners of the test panel [14].

Fig. 11. Photograph of IR camera used at the testbed to capture backside temperatures [3], [14]

The testbed was also instrumented with an IR camera that created video recordings during the lightning tests, to measure the backside temperatures during the lightning strike. IR images were later extracted, as individual frames, from the video recordings. The purpose of the IR images was to show temperatures at the lightning attachment locations and along the current pathways from resistive heating. Fig. 11 shows a photograph of the IR camera positioned on the back side of the test panel.

B. MODELING AND SIMULATIONS

1) Software

Modeling and simulation of electromagnetic phenomena is an indispensable tool at any stage and for any scale of an electrical engineering research problem. For this investigation, a computational electromagnetic software tool called FEldberechnung für Körper mit beliebiger Oberfläche (FEKO), which is German for "Field Calculations for Bodies with Arbitrary Surface," was used to develop these simulations [38]. FEKO develops computational solutions that use Method of Moments (MoM), a technique that

estimates the population parameters, to compute full wave solutions on integral formulations of Maxwell's equations in the frequency domain [38], [39].

2) Computational Hardware

The simulations ran on a 64-bit Windows 7 operating system machine with an Intel Xeon central processing unit (CPU) E5-1650 that ran at a clock speed of 3.20 gigahertz (GHz) and had 32 gigabytes (GB) of installed random access memory (RAM) [3].

3) Models and Simulations

In CAD FEKO, the SansEC LSP test panels were created and designed. CAD FEKO was also used to define SansEC sensors' and other panel parameters' material and geometric properties.

The simulated test panels were created with the parameters specified in Table 3.

TABLE 3. PARAMETERS OF MODELED SANSEC LSP TEST PANELS

SansEC Parameters	7-inch	8-inch	9-inch
Relative Permittivity (ε_r)	∞		
Trace Width	93.75 mils		
Trace Gap Width	31.25 mils		
Material Thickness	1.25 mils		
Dimensions	7 in. x 7 in.	8 in. x 8 in.	9 in. x 9 in.
Ground Paths Parameters			
Relative Permittivity (ε_r)	∞		
Material Thickness	1.25 mils		
Dimensions (4 inner)	2 in. x 13 in.		
Dimensions (4 outer)	1 in. x 18 in.		
FRP Parameters			
Dielectric Loss Tangent (Tanδ)	0.017		
Relative Permittivity (ε_r)	4		
Mass Density	1850 kg/m^3		
Material Thickness	0.15 in.		
Dimensions	20 in. x 20 in.		
Dielectric Paint Parameters			
Relative Permittivity (ε_r)	2.5		
Mass Density	1198.26 kg/m3		
Material Thickness	4 mils		
Dimension Coverage	20 in. x 20 in.		

The simulated panels, as shown in Fig. 12, were constructed with 0.15-inch thick FRP defined by a relative permittivity ε_r of 4, a loss tangent Tanδ of 0.017, and a mass density of 1850 kg/m^3 [3]. Although the FRP of the panel was 0.25 inches, the FRP of the panel was simulated at 0.15 inches to simplify computation [3]. The conductive ground paths that encompassed the edges of the panel of the 7-inch, 8-inch and 9-inch SansEC sensors were accurately modeled in the geometries [3]. The endpoint of the sensor spiral trace was always positioned at the lower right corner of the panel, with the trace proceeding in a clockwise manner to the center. The dielectric paint over the test panel was modeled

with a ε_r of 2.5 and mass density of 1198.26 kg/m^3 [3]. The computational model did not include a primer layer under the paint, which was used in the experimental model [3].

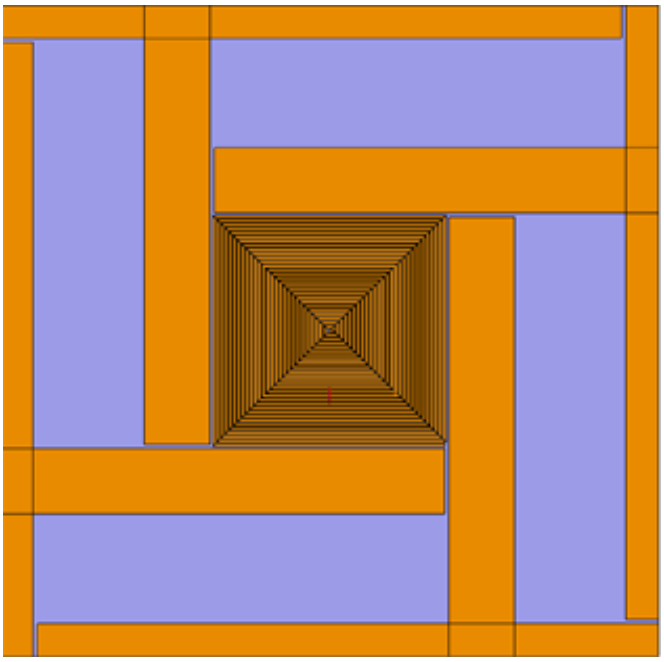

Fig. 12. FEKO Model of the LSP Test Panel (shown unpainted) [3]

Once the parametric creation of the models was completed, the geometries meshed as triangles, segments, and connections points, all of which were frequency dependent [38], [39].

An electromagnetic field is hypothesized to precede an actual lightning strike leader [3]. To simulate the resonant sensor to mimic this environment, a 4-inch square loop antenna was positioned 0.5 inches above the sensor on each modeled panel as illustrated in Fig. 13. The antenna was used to excite the SansEC sensor by creating 1 volt electromagnetic signal that propagated from 0 MHz to 300 MHz.

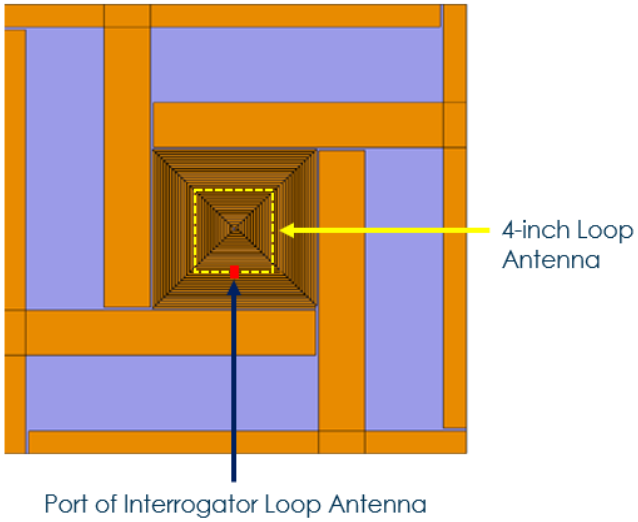

Fig. 13. FEKO Model of the LSP Test Panel with Antenna and Port outlined and labeled [3]

The matrix elements were based on the parametrized triangle meshes at various locations on the model [14]. MoM was used to solve full wave integral formulations of Maxwell's equations in the frequency domain for each triangle of the mesh at select points [38] [39]. MoM provided vector solutions to the linear set of Maxwell's equations. The matrix was decomposed into a product of matrices, followed by backward substitutions that provided the solutions of the models, such as surface currents, electric and magnetic fields, impedance, and power amplitude as a function of frequency [14], [40], [41]. The computational simulations also calculated the readback response from the loop antenna modeled as S11, which gave us the reflection coefficient [38].

CHAPTER IV

RESULTS AND ANALYSIS*

A. LIGHTNING TEST RESULTS

The measured electric current was taken from the four Pearson 4418 current probes at the time of lightning strike. The raw data collected from the current probes was exported to comma-separated values (.csv) files. The .csv files were later imported into DADiSP, a scientific computing and data visualization software, and processed [42]. The measured electric current plots shown in this thesis were created using DADiSP.

IR images were extracted, as individual frames, from the video recordings from the IR camera. The IR images shown in this thesis were frames taken from the 7-inch, 8-inch, and 9-inch SansEC LSP configuration at 4 seconds (sec) after the lightning strike. The purpose of the IR images was to show high temperatures at the lightning attachment locations and along the current pathways from resistive heating.

1) 7-Inch SansEC

The measured electric currents from the 7-inch SansEC LSP configuration are shown in Fig. 14. Fig. 14 displays the current amplitude in kA, with respect to time in milliseconds (ms) and shows that all the electrical current traveled in channels 2 and 3. The second amplitude peak visible in the unipolar waveform at 0.1 ms is an artifact of a resistor flashover short in the resistor bank of the lightning current generating system during the strike [3]. A flashover is the near-instantaneous combustion of a directly exposed

*Portions of this research were previously presented at the International Conference on Lightning and Static Electricity (ICOLSE) 2013 in Seattle, Washington [3].

inflammable material in an encased or compacted space [43], [44]. A resistor flashover short occurs when a semi or moderately conductive material is exposed to high electric fields; when certain materials are heated, the materials undergo thermal breakdown and expel inflammable vapors that discharge [43], [44]. These localized vapors discharge and disrupt the flow of charges, potentially altering current data collected during a lightning experiment [43], [44].

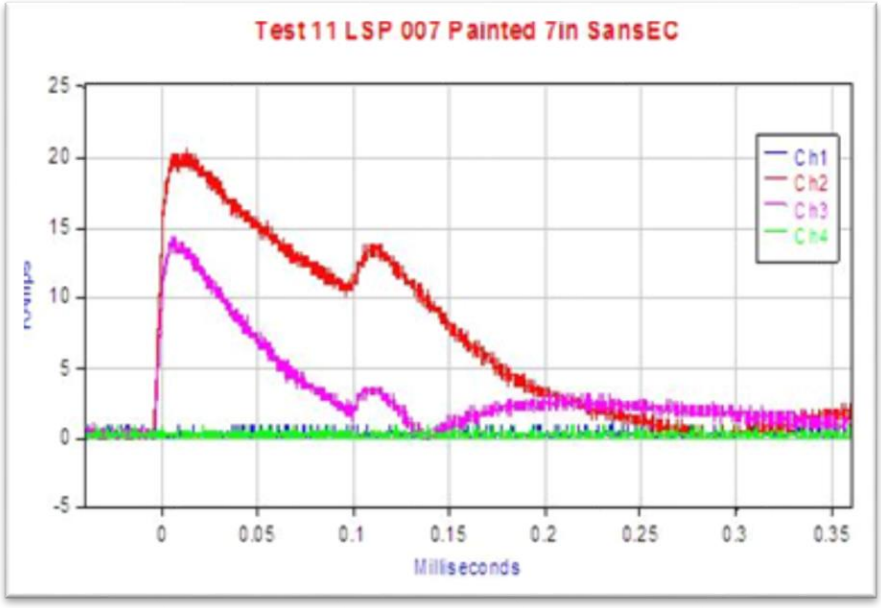

Fig. 14. Measured Electric Currents on 7-inch SansEC [3], [14]

Fig. 15 on the left shows a photograph of the post-strike panel with a graphical representation of the ground paths to identify the current channels. Channel 2 is attached to the left edge of the panel and is attached to the ground path beneath the SansEC in the picture [3]. Channel 3 is on the bottom edge and is attached to the ground path on the right

side of SansEC in the picture [3]. Electric current exiting the bottom right corner of the SansEC could become attached to ground by either channel 2 or 3 [3]. The action integral was calculated for each channel to determine the ratio of energy along each path. Channel 2 showed 80% of the total energy and channel 3 showed 20% [3].

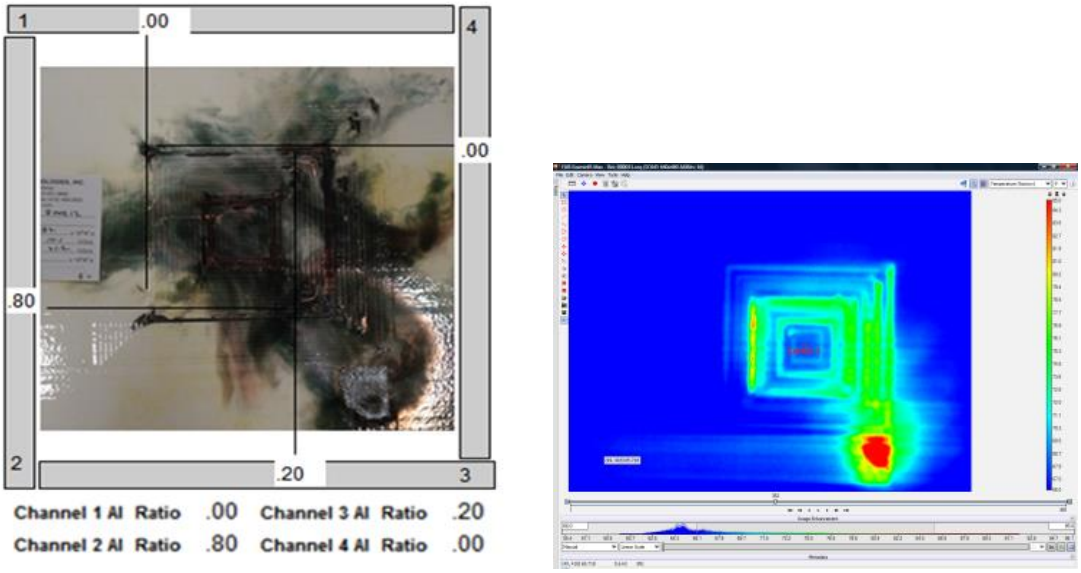

Fig. 15. 7-inch SansEC panel post-lightning strike damage on left and IR image on right [3], [14]

A thermal image of the 7-inch SansEC LSP configuration is shown in Fig. 15 on the right. The IR images were inverted to represent a front side depiction since the thermal data was collected from the back side of the testbed [3]. The hotter temperatures represent the location of lightning attachment or current propagation [3]. If a portion of the SansEC trace is immediately destroyed/removed from the panel the IR image may not sense an increase in temperature at that location [3]. Fig. 15 shows high temperatures at the intersection of the ground paths attached to channel 2 and 3 at the lower right corner of the

SansEC sensor in red, yellow, and green, respectively [3]. Even though the sensor is electrically conductive everywhere, the resistive heating did not occur uniformly over the sensor traces [3]. Note the absence of resistive heating in the center of the sensor [3]. On the right side of the sensor, five separate traces appear to have high temperatures [3].

2) 8-Inch SansEC

The measured electric current for the 8-inch SansEC LSP configuration is shown in Fig. 16. All the lightning current was measured in channel 2 [3]. The second amplitude peak around 0.075 ms was again caused by a resistor flashover short [3].

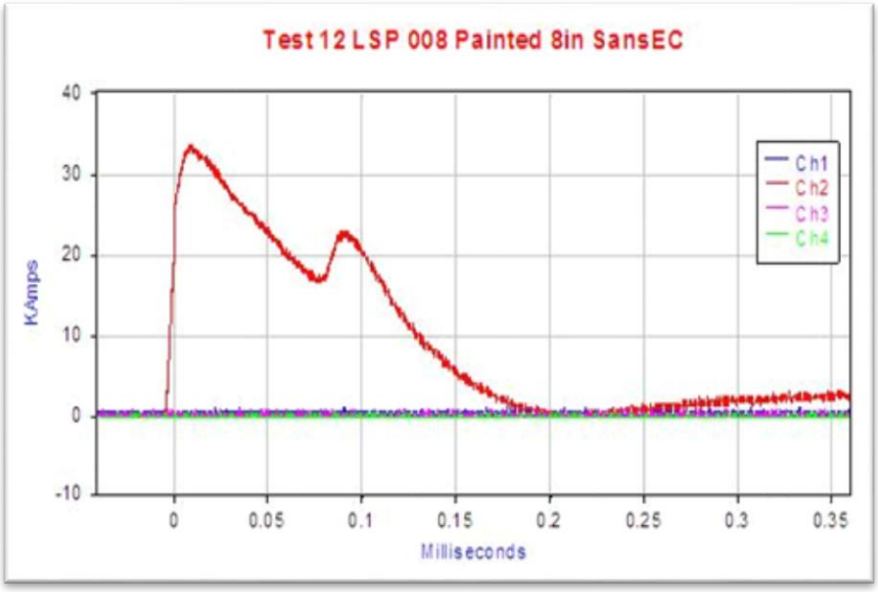

Fig. 16. Measured Electric Currents on 8-inch SansEC [3], [14]

A photograph of the post-strike panel and graphical representation of the ground paths with action integral percentages are shown in Fig. 17 on the left. Burnt traces on the

sensor and ground paths can be seen in the picture [3]. The action integral was calculated and channel 2 showed 100% of the total energy [3].

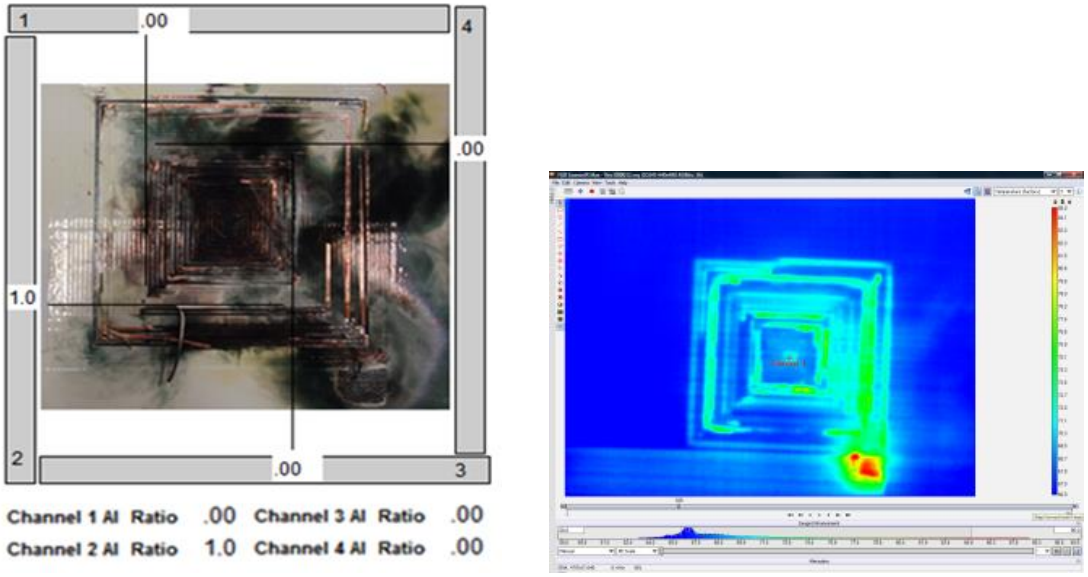

Fig. 17. 8-inch SansEC panel post-lightning strike damage on left and IR image on right [3], [14]

The IR image for this test configuration is shown in Fig. 17 on the right. The ground path for channel 2 has the highest temperature values [3]. The image is similar in nature to the 7-inch IR image but with six traces on the right side showing high temperatures [3].

3) 9-Inch SansEC

The measured electric current for the 9-inch SansEC LSP configuration is shown in Fig. 18. All the lightning current once again was measured in one channel but in this case channel 3 [3]. The second amplitude peak around 0.125 ms is visible in the data from the resistor flashover short [3]. The action integral was calculated and channel 3 showed 100% of the total energy [3].

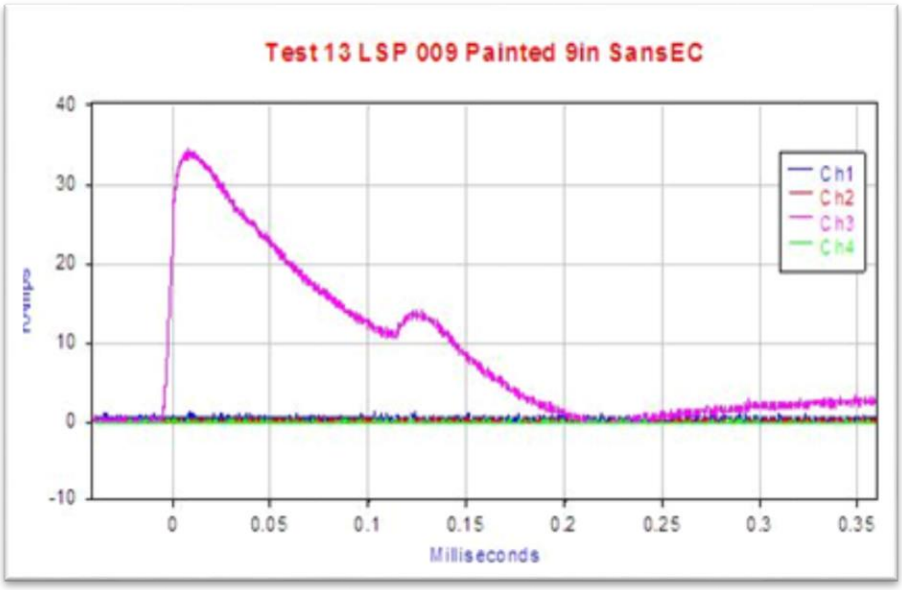

Fig. 18. Measured Electric Currents on 9-inch SansEC [3], [14]

A photograph of the 9-inch LSP configuration post-strike panel and graphical representation of the ground paths with action integral percentages are shown in Fig. 19 on the left. The picture shows burn marks at the upper right corner of the 9-inch sensor [3].

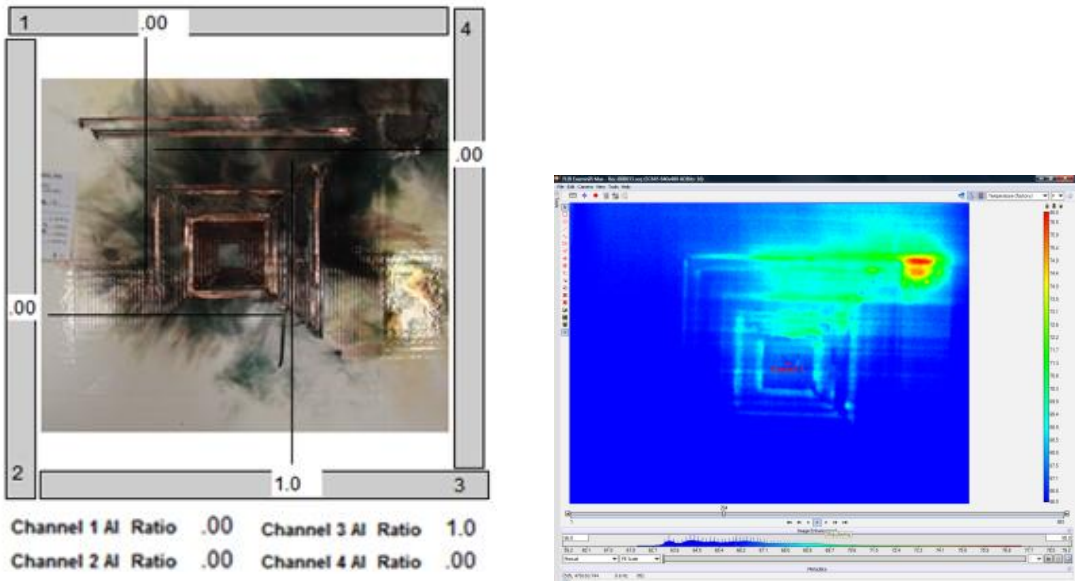

Fig. 19. 9-inch SansEC panel post-lightning strike damage on left and IR image on right [3], [14]

The IR image for this test configuration is shown in Fig. 19 on the right. The ground path for channel 3 has the highest temperature values [3]. The image shows much more heating across the top portion of the sensor's traces than in the other two configurations [3]. On the top right side of the sensor, four separate traces appear to have high temperatures [3].

A summary of the lightning strike test results is shown in Table 4**.**

TABLE 4. SUMMARY OF POST-LIGHTNING STRIKE PANEL DAMAGE

SansEC Configuration	**Location of Energy Steering on Panel**	**Channels that Measured Lightning Current**
7-inch	Lower Right Corner	Channel 2 & Channel 3
8-inch	Lower Right Corner	Channel 2
9-inch	Upper Right Corner	Channel 3

From observing the IR images and damaged panels, it appears that the 7-inch and 8-inch SansEC both exhibited the same behavior of steering the lightning energy to the lower right corner of the panel [3]. The 9-inch SansEC displayed similar behavior but steered the lightning energy towards the upper right corner of the panel [3]. The lightning current, measured from the current probes, traveled in channel 3 in each configuration but traveled in channel 2 as well, for the 7-inch SansEC [3].

B. SIMULATION RESULTS

In this study, both the real and imaginary reflection coefficient values were observed, but only the real values were shown to provide more insight on lightning attachment.

1) 7-Inch SansEC

The 7-inch SansEC sensor reflection coefficient plot, displaying amplitude in decibels (dB) as a function of frequency in megahertz (MHz), is shown in Fig. 20. The primary resonance frequency is at approximately 57 MHz at a level of -26 dB [3]. The second largest resonance occurs just below 48 MHz at -14 dB [3]. These are strong resonances and are more than adequate to perform sensing in an FRP. Strong resonance phenomena diminish above 100 MHz [3].

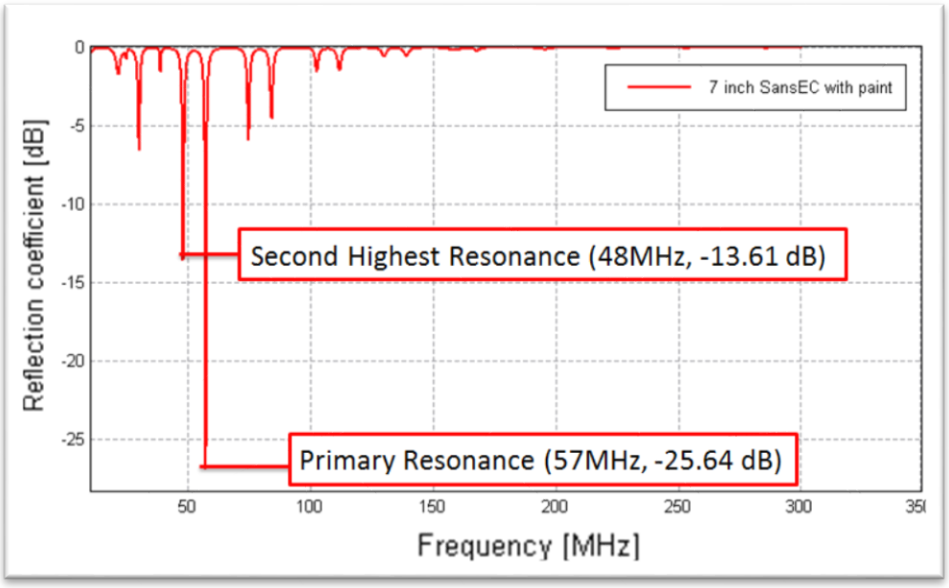

Fig. 20. Reflection Coefficient of the 7-inch SansEC [3], [14]

Fig. 21 presents the electric and magnetic field distribution in dBV/m and dBA/m respectively for the 7-inch SansEC sensor. The simulations contained the full panel with grounds, but only the SansEC sensor fields are presented [3]. The amplitude scales were selected to provide visual contrast between high field regions and low field regions [3]. Fig. 21 on the left clearly shows five distinctive loops of relatively higher electric field at the primary resonance frequency [3]. Fig. 21 on the right shows four distinct loops of relatively higher magnetic field also at the same frequency [3]. Note both images have no significant field strength at the center of the spiral and at the outer end of the spiral [3]. The open circuit nature of the SansEC sensor requires no current flow at the end of the trace and thus the field strength diminishes to zero [3].

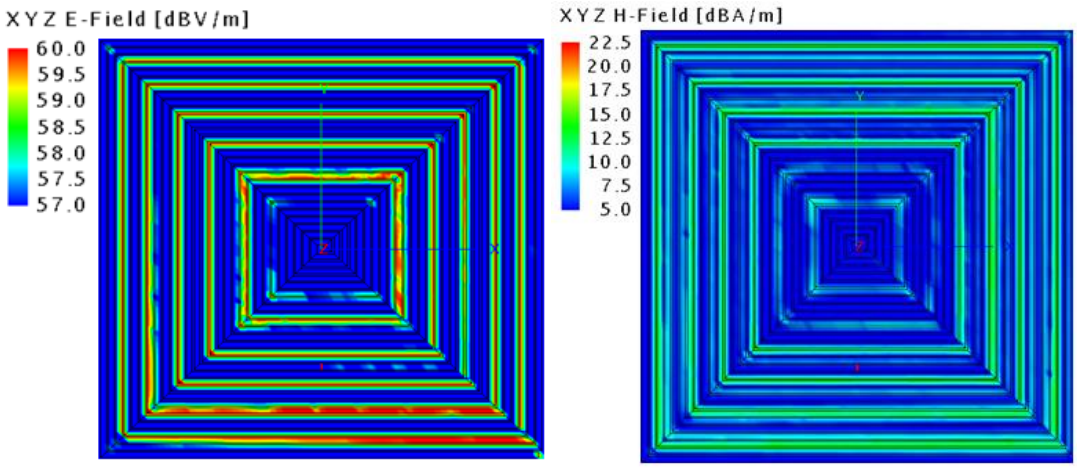

Fig. 21. E-field and H-field of 7-inch SansEC at primary resonance, 57 MHz [3], [14]

2) 8-Inch SansEC

The 8-inch SansEC reflection coefficient versus frequency plot is shown in Fig. 22. The primary resonance of the 8-inch SansEC sensor is -21 dB at approximately 51 MHz [3]. The second highest resonance is about -14 dB at approximately 58 MHz [3]. Strong resonance phenomena diminish above 100 MHz [3].

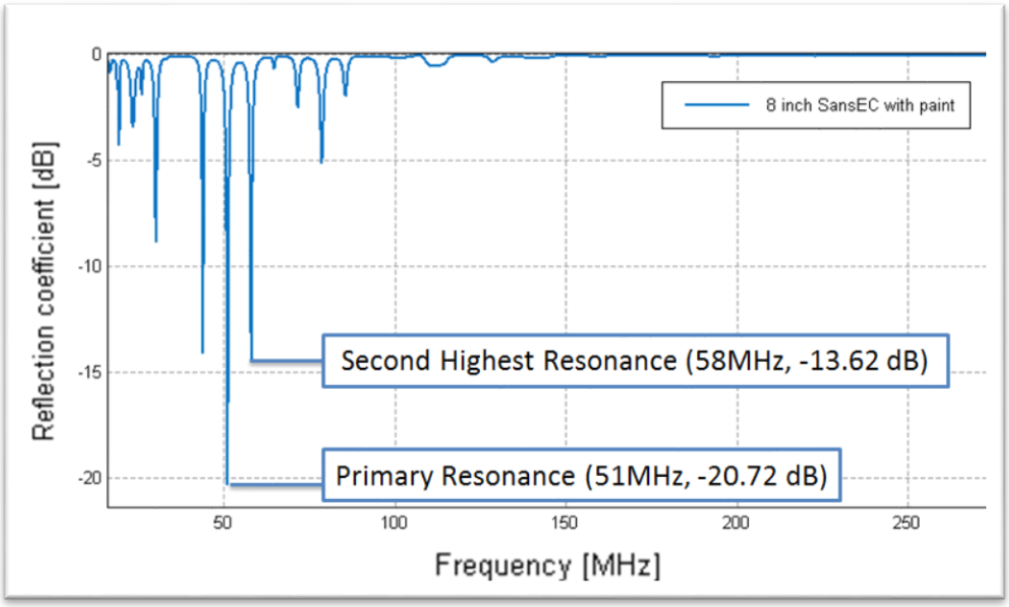

Fig. 22. Reflection Coefficient of the 8-inch SansEC [3], [14]

Fig. 23 presents the electric and magnetic field distribution for the 8-inch SansEC sensor at 51 MHz in the same format as presented for the 7-inch [3]. The electric field distribution shows six loops with relatively higher fields while the magnetic field distribution shows five [3].

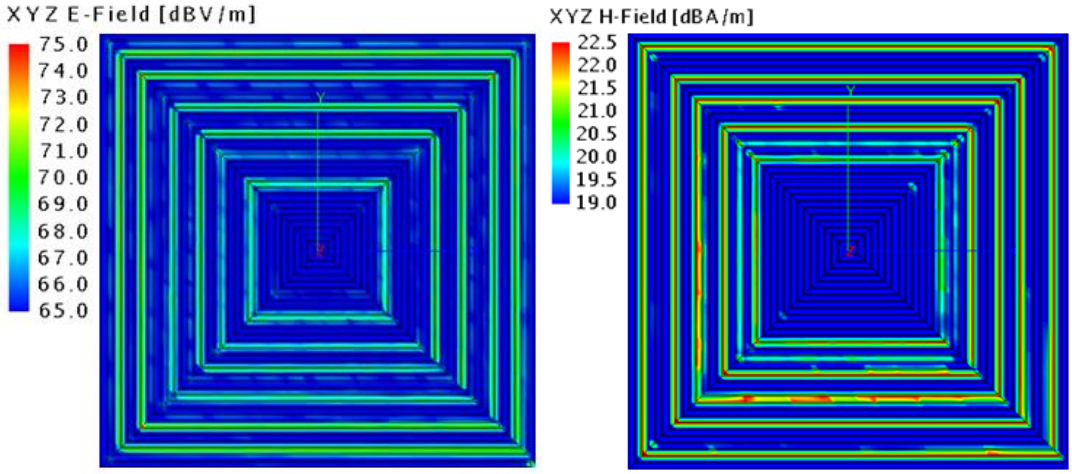

Fig. 23. E-field and H-field of 8-inch SansEC at primary resonance, 51 MHz [3], [14]

3) 9-Inch SansEC

The 9-inch SansEC reflection coefficient versus frequency plot is shown in Fig. 24. The primary resonance of the 9-inch SansEC sensor is -34 dB at approximately 52 MHz [3]. The second highest resonance is around -15 dB at approximately 58 MHz [3]. Again, strong resonance phenomena diminish above 100 MHz [3].

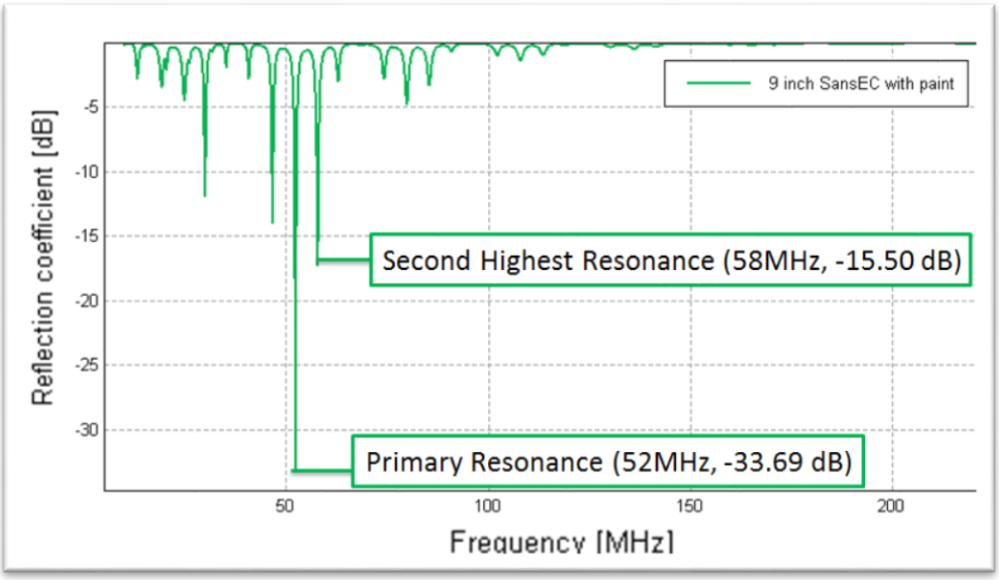

Fig. 24. Reflection Coefficient of the 9-inch SansEC [3], [14]

Fig. 25 presents the electric and magnetic field distribution for the 9-inch SansEC sensor at 52 MHz in the same format as presented earlier [3]. The electric field distribution again shows six distinctive loops with relatively higher electric field [3]. The magnetic field distribution does not show the distinctive loops of relatively higher magnetic field regions as was observed in the 7-inch and 8-inch sensors [3]. Instead, it appears that nearly all the traces of the 9-inch sensor generate magnetic field activity at the resonance frequency [3]. The center of the spiral and outer edge is still shown to have a minimal magnetic field [3].

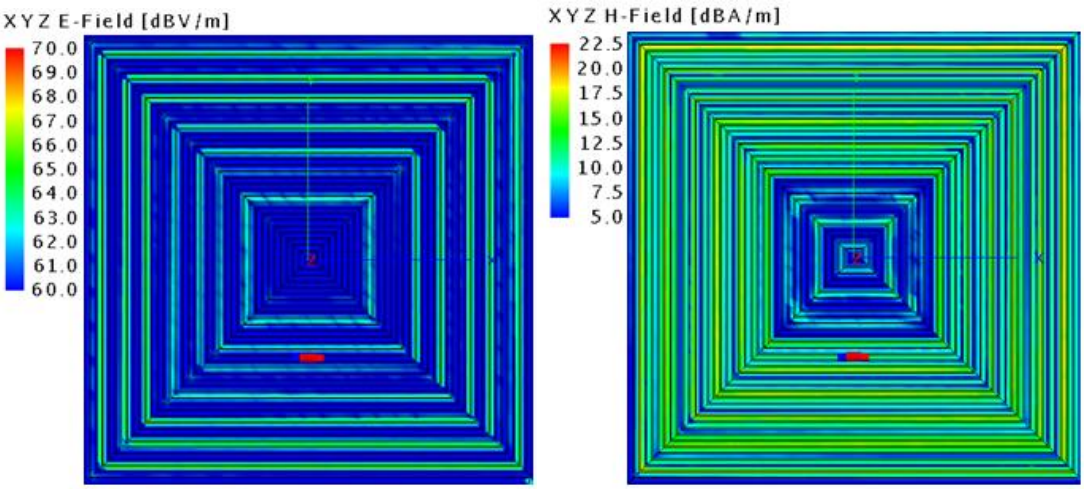

Fig. 25. E-field and H-field of 9-inch SansEC at primary resonance, 52 MHz [3], [14]

A summary of the simulation results is shown in Table 5**.**

TABLE 5. SUMMARY OF RESONANCE FREQUENCIES 7 IN., 8 IN., AND 9 IN. SANSEC

	Resonance Frequencies	
SansEC Configuration	**Primary Resonance (MHz)**	**Second Resonance (MHz)**
7-inch	57	48
8-inch	51	58
9-inch	52	58

Electromagnetic simulations were conducted to determine each sensor configurations' primary resonance frequency, which was found to be at 57 MHz, 51 MHz, and 52 MHz for the 7-inch, 8-inch, and 9-inch configurations, respectively. The electric and magnetic field distributions were mapped just above the surface of the SansEC sensor's conductive trace at its primary resonance.

C. COMPUTATIONAL RESULTS

As mentioned in the Methodology Section III.B.2, the simulations ran on a 64-bit operating system computer with an Intel Xeon CPU E5-1650 that ran at a clock speed of 3.20 GHz and had 32 GB of installed RAM [3].

The simulation run times with corresponding SansEC configurations are shown in Table 6.

TABLE 6. COMPUTATIONAL RUN TIME FOR SIMULATIONS

SansEC Configuration	Number of Points	Simulation Run Time
7-inch	300	03:59:05
8-inch	300	07:47:19
9-inch	300	19:01:35

The simulation total run time for the 7-inch was 3 hours: 59 minutes: 5 seconds and it used approximately 242.744 megabytes of memory per process [3]. The total run time for the 8-inch simulation was 7 hours: 47 minutes: 19 seconds and it used approximately 295.194 megabytes of memory per process [3]. The total run time for the 9-inch was 19 hours: 1 minute: 35 seconds and it used approximately 976.457 megabytes of memory per process [3]. For each simulation, 300 points were requested from the triangle meshes of the model to sufficiently identify the electric and magnetic field structure of the SansEC sensors in the study presented in this thesis.

D. CORRELATIONAL ANALYSIS

The correlational analysis presented in this study is both qualitative and quantitative. For the qualitative analysis, portions of the IR images were cropped and pasted over the electric field distribution images to help visually align the location of the hotter traces next to the relatively higher electric field traces. For the quantitative analysis, both the IR images and electric field distribution images were converted to grayscale, converted to double precision, cropped to only show the SansEC sensor, and resized to be of the same image dimensions/size of the corresponding sensor configuration [45].

The structural similarity index (SSIM) and the peak signal to noise ratio (PSNR) were calculated for portions of the IR and electric field distribution images shown qualitatively correlated in this section. SSIM is a measure of similarity of two images using statistical parameters mean and variance [46]. The calculated SSIM returns a scalar value that ranges between 0 to 1, where 1 suggests strong similarities and 0 suggests weak to no similarities [46]. The PSNR is another measure of similarity using mean squared error (MSE) [46], [47]. MSE is a statistical method for measuring the deviations of two quantities [46], [47]. The calculated PSNR returns a scalar value in dB, where above 20dB suggests strong similarities, 20dB-15dB suggests adequate similarities, and below 15dB suggests weak similarities [47].

The IR images and electric field distribution images were further processed and massaged to eliminate artifacts that would impact the image similarity comparison. A Gaussian filter, of size $\sigma = 4$, was applied to the electric field distribution images to eliminate the trace of the sensor (high frequency image components) that were not present

in the IR images [48]. A histogram equalizer was applied to the IR images to transform the image contrast to that of the electric field distribution image [48].

The image processing and quantitative analysis for this study were done in Matrix Laboratory (MATLAB version 2017a) using the Image Processing Toolbox [48].

1) 7-Inch SansEC

The electric field distribution of the 7-inch SansEC conductive trace at the primary resonance is shown appropriately sized next to the 7-inch lightning test IR image in Fig. 26 [3]. A slice of the IR image from above the center line has been pasted over the electric field distribution to help visually align the location of the hotter traces next to the relatively higher electric field traces [3]. The five high electric field traces on the right side of the electric field distribution seem to align well with the five high temperature traces on the right side of the IR image [3]. The area of low electric field, in the center of the electric field distribution, appears to coincide with the area of low temperature in the IR image [3]. High electric field regions occurring at other resonant frequencies are not studied here, but could also play a role in lightning attachment to the sensor [3].

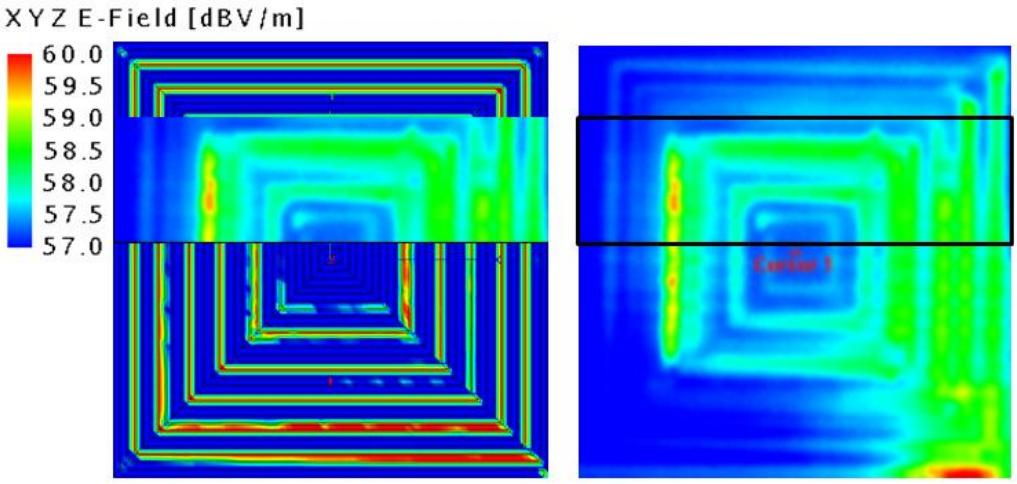

Fig. 26. 7-inch SansEC E-field at 57 MHz compared with IR image [3], [14]

The SSIM index and PSNR calculated for the 7-inch IR image and electric field distribution image, shown correlated in Fig. 26, was 0.29 and 17.2 dB, respectively.

2) 8-Inch SansEC

The electric field distribution of the 8-inch SansEC conductive trace at the primary resonance is shown appropriately sized next to the 8-inch lightning test IR image in Fig. 27 [3]. A slice of the IR image from above the center line has been pasted over the electric field distribution to help visually align the location of the hotter traces next to the relatively higher electric field traces [3]. The six high electric field traces on the right side of the electric field distribution seem to approximate the location of the six high temperature traces on the right side of the IR image [3]. The area of low electric field, in the center of the electric field distribution, is reasonably close to the area of low temperature in the IR image [3].

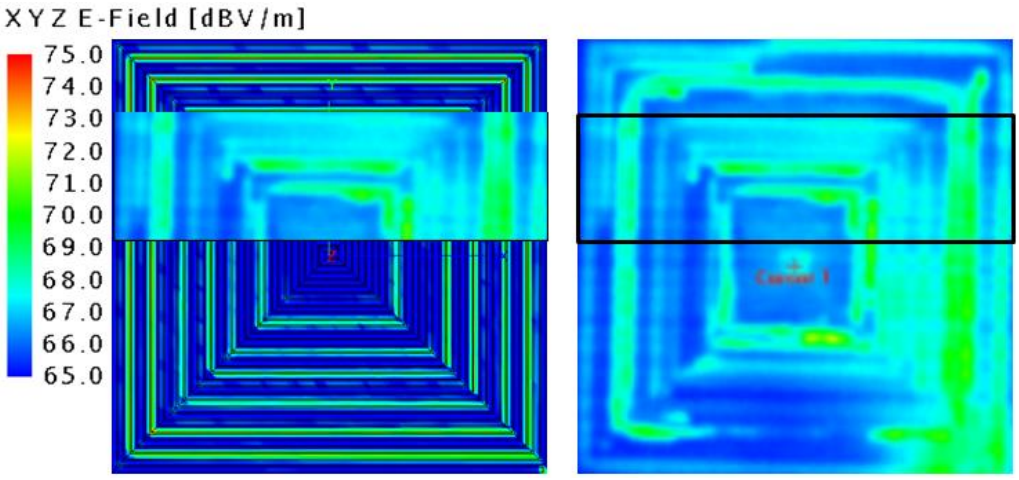

Fig. 27. 8-inch SansEC E-field at 51 MHz compared with IR image [3], [14]

The SSIM index and PSNR calculated for the 8-inch IR image and electric field distribution image, shown correlated in Fig. 27, was 0.38 and 18.3 dB, respectively.

3) 9-Inch SansEC

The electric field distribution of the 9-inch SansEC conductive trace at the primary resonance is shown appropriately sized next to the 9-inch lightning test IR image in Fig. 28 [3]. A portion of the IR image from the upper left corner has been pasted over the electric field distribution to help visually align the location of the hotter traces in this area next to the relatively higher electric field traces [3]. The traces above center line appear to align reasonably well and are in good agreement at the upper left loop corners [3]. The area of low electric field, in the center of the electric field distribution, is reasonably similar to the area of low temperature in the IR image [3].

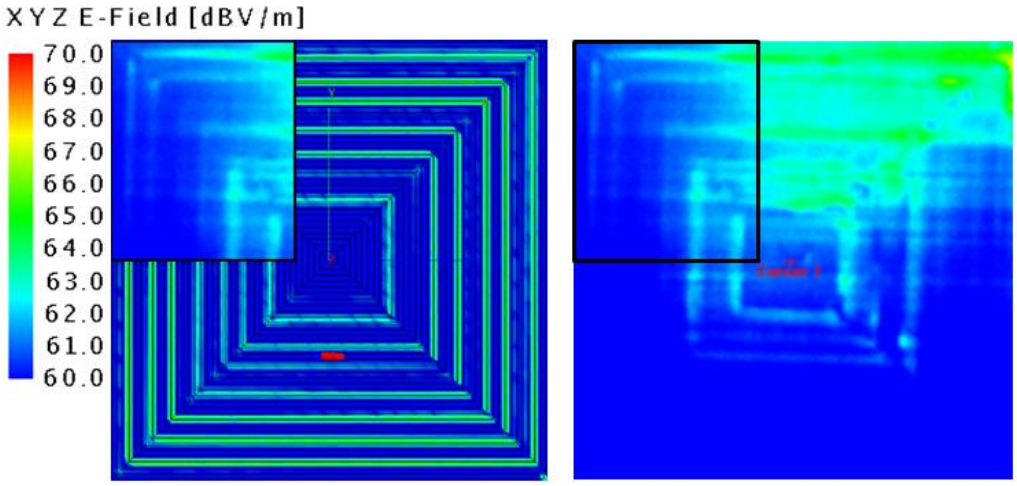

Fig. 28. 9-inch SansEC E-field at 52 MHz compared with IR image [3], [14]

The data represented in Fig. 28 are repeated and shown in Fig. 29 with a different dBV/m scale to further show correlation [3], [14].

The SSIM index and PSNR calculated for the 9-inch IR image and electric field distribution image, shown correlated in Fig. 28, was 0.55 and 18.7 dB, respectively.

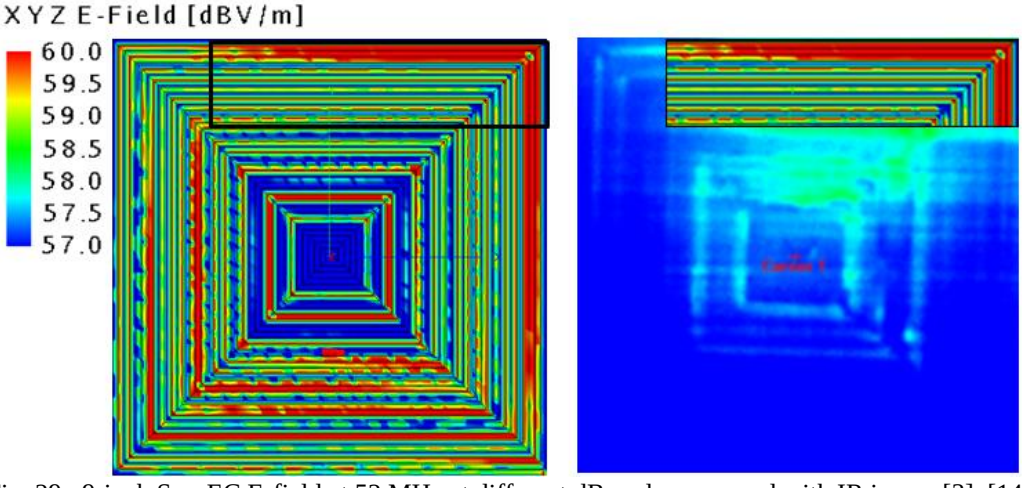

Fig. 29. 9-inch SansEC E-field at 52 MHz at different dB scale compared with IR image [3], [14]

The dB scale has been compressed to highlight the high electric field regions appearing at the upper right corner [3]. A slice of the electric field distribution from the upper right corner is shown overlaid on the IR image [3]. The electric field distribution shows very high relative field values at this corner and corresponds to the high temperatures shown in the IR image [3].

TABLE 7. IR & E-FIELD IMAGE SIMILARITY MEASURED IN SSIM AND PSNR

SansEC Configuration	**Structural Similarity (SSIM) Index**	**Peak Signal to Noise Ratio (PSNR), dB**
7-inch (Fig. 26)	0.29	17.2
8-inch (Fig. 27)	0.38	18.3
9-inch (Fig. 28)	0.55	18.7

Table 7 shows the calculated SSIM and PSNR results. The calculated SSIM and PSNR for the 7-inch, 8-inch, and 9-inch configurations were in the range of adequate similarities, 0.29, 0.38, and 0.55 and 17.2 dB, 18.3 dB, and 18.7 dB, respectively.

Both the qualitative and quantitative results showed a correlation between the IR image and the electric field distribution image.

CHAPTER V

CONCLUSION AND FUTURE WORK*

Old Dominion University and NASA Langley Research Center conducted research to develop sensors to provide LSP and damage mitigation for composite aircraft.

Lightning-direct effect current tests were conducted on multiple SansEC sensor configurations on FRP substrates [3]. The frequency content of a lightning waveform falls within the operational frequency resonance bands for these sensor configurations that were tested [3]. As the lightning arc propagates toward the test panel its radiated electromagnetic field generates a self-resonance on the sensor establishing electric and magnetic field modal structures on the sensors' spiral trace [3]. Test results have shown the 7-inch, 8-inch, and 9-inch square sensor configurations have an intrinsic ability to guide the lightning energy in one direction based on test results from current measurements made on the four sides of the test panels and back side IR imagery [3]. IR temperature measurements provide a visual means to show electrical resistive heating from lightning attachment and current propagation on the sensor geometry [3].

Electromagnetic simulations were conducted using FEKO to determine the sensor's primary resonance frequency and to visualize the electric and magnetic field structure residing on the sensor trace at primary resonance [3]. Those visualization mappings were then compared qualitatively and quantitatively to the IR images to correlate high field strength with lightning attachment and propagation [3].

---

*Portions of this research were previously presented at the International Conference on Lightning and Static Electricity (ICOLSE) 2013 in Seattle, Washington [3].

The electric field distribution images were compared to the lightning test IR image to correlate the locations of high electric fields to the high temperatures seen in the IR image [3]. All three sensors, qualitatively and quantitatively, showed a reasonable correlation between the high electric field regions to the locations with high temperatures and lightning attachment or current propagation. It is noted that traces that have been immediately burned away or destroyed would not show increased temperatures in the IR image [3].

These correlation results suggest that high electric field regions on the sensor at resonance influence the attachment and propagation of the lightning energy and that the lightning attachment on the sensor occurs at the high electric field regions resident on the conductive trace at its primary resonance frequency [3]. Higher relative electric fields at other resonance frequencies may also influence attachment but were not included in this study [3].

This correlational study provides a better understanding of the sensors' behavior in a lightning environment and in the functionality of steering lightning current from an attachment or detachment point to a less critical point on an in-flight aircraft.

Moreover, based on the results and analysis of this investigation, further research should be conducted to understand the behavior of other SansEC sensor configurations of different sizes, shapes, and materials in a lightning environment. Once more individual sensors of different configurations are better understood, the sensors can be further studied as functional arrays known as Smart Skins [1], [2], [14]. The main concept is to apply these sensor arrays to an aircraft surface and thus forming a Smart Skin layer as an external or embedded protective layer as shown in Fig. 30 [1], [2], [14].

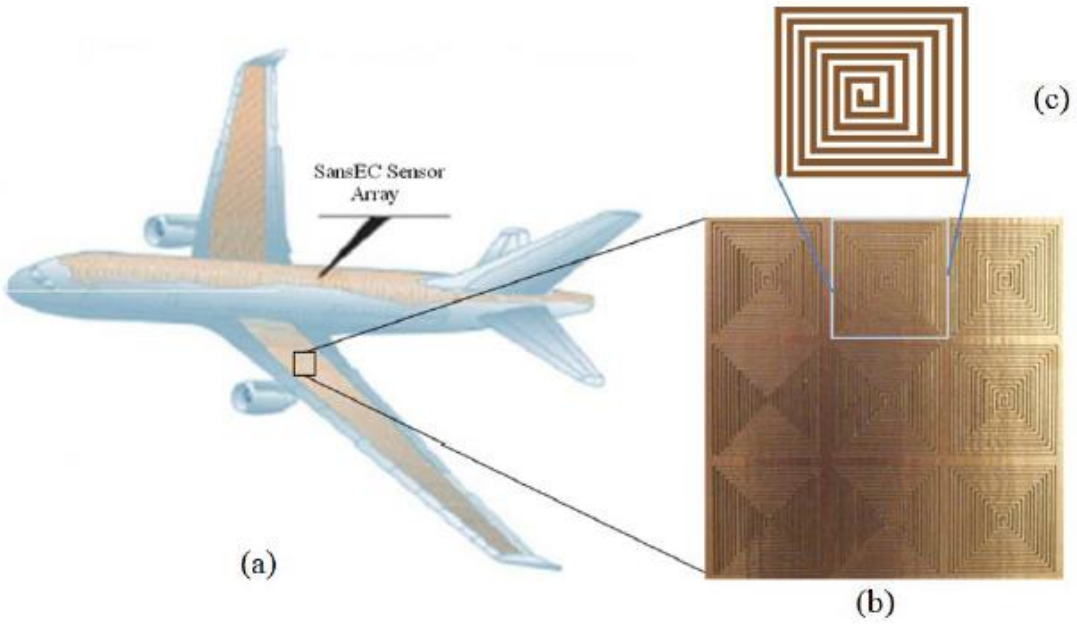

Fig. 30. (a) SansEC Smart Skin on an aircraft (b) a SansEC Array (c) a single SansEC [14]

The Smart Skin technology could provide shielding effectiveness, lightning strike protection, and the opportunity to achieve local damage detection and diagnostics for aerospace composite structures along with other potential beneficial functions not available from the standard LSP method [1], [2], [4].

Aircraft incorporating Smart Skin technology is a very viable concept and could be realized from two different approaches. One approach is for the on-site measurements, where the sensors would be embedded within, on top of or underneath the composite and directly wired to onboard instruments that would quantify and measure the state of structural health of the aircraft [1], [2]. In this method, the sensors' response is monitored in real-time during the flight. After a lightning strike occurs, the interrogation system could

scan the sensor array and compare the scanning result with the nominal baseline stored in a database or utilize an algorithm capable of determining a damaged state without baseline reference to determine the health state of the vehicle [1], [2]. Another approach would be to have an external interrogation system at the hanger or the aircraft maintenance facility. This external interrogation system would measure the state of structural health of the aircraft by using the Smart Skin to assess and detect potential damage and assist inspections [1], [2], [14]. Ideally, this method would be for routine aircraft health checks post flight when specific incidents such as a suspected or known lightning strike occur [14].

REFERENCES

[1] C. Wang, K. Dudley, G. Szatkowski, "Open Circuit Resonant (SansEC) Sensor for Composite Damage Detection and Diagnosis in Aircraft Lightning Environments," American Institute of Aeronautics and Astronautics, 8, Jun. 25, 2012

[2] S. Woodard, "SansEC Sensing Technology - A New Tool for Designing Space Systems and Components", Aerospace Conference, 2011.

[3] K. M. Farrow, “International Conference on Lightning and Static Electricity (ICOLSE),” in Correlational Study of Open Circuit Resonant (Sansec) Sensor's Electric Field Distribution on Lightning Attachment, Sept. 2013. [Online]. Available: https://digitalcommons.odu.edu/ece_fac_pubs/127

[4] C. Rash, "When Lightning Strikes: Aircraft Designs Incorporate Systems to Protect Against Direct and Indirect Damage,” Flight Safety Foundation, pp. 1, 2011.

[5] P. J. Filho and U. Z. Khan, “International Conference on Lightning & Static Electricity (ICOLSE),” in Analysis of Impact Damage by Lightning Strikes on Aircraft CFC Structures, 2015.

[6] J.-F. Boissin and F. Flourens, “2012 ESA Workshop on Aerospace EMC 2012,” in Proceedings of the 2012 ESA Workshop on Aerospace EMC 2012, 2012.

[7] “Trans World Airlines L1649A,” 15-Nov-1960. [Online]. Available: http://lessonslearned.faa.gov/PanAm214/TWA_L1649A_AccReport.pdf. [Accessed: 28-Oct-2017].

[8] F. A. Administration, “Accident Overview,” Lessons Learned. [Online]. Available: http://lessonslearned.faa.gov/ll_main.cfm?TabID=4&LLID=46&LLTypeID=2. [Accessed: 27-Oct-2017].

[9] S. Williams, “Sole Survivor: The Woman Who Fell to Earth,” The Telegraph, 22-Mar-2012. [Online]. Available: http://www.telegraph.co.uk/culture/books/authorinterviews/9143701/Sole-survivor-the-woman-who-fell-to-earth.html. [Accessed: 26-Oct-2017].

[10] H. Ranter, “ASN Aircraft Accident Swearingen SA227-AC Metro III D-CABB Kettwig,” Aviation Safety Network, 08-Feb-1988. [Online]. Available: http://aviation-safety.net/database/record.php?id=19880208-2. [Accessed: 28-Oct-2017].

[11] H. Ranter, “ASN Aircraft Accident Xian Yunshuji Y-7-100C B-3479 Wuhan,” Aviation Safety Network, 22-Jun-2000. [Online]. Available: https://aviation-safety.net/database/record.php?id=20000622-0. [Accessed: 28-Oct-2017].

[12] C. Featherston, M. Eaton, S. Evans, "Development of a Methodology to Assess Mechanical Impulse Effects Resulting from Lightning Attachment to Lightweight Aircraft Structures," Applied Mechanics and Materials, Vol. 24-25, no. , 129-134, 2010.

[13] “Carbon Fibre Reinforced Composites,” Plus Composites. Plus Composites. [Online]. Available: http://www.pluscomposites.eu/sites/default/files/Technical%20series%20-%20Part%204%20-%20Carbon%20fibre%20reinforced%20composites_0.pdf

[14] G. Szatkowski, "Open Circuit Resonant (SansEC) Sensor Technology for Lightning Mitigation and Damage Detection and Diagnosis for Composite Aircraft Applications," NASA Technical Publication, Nov.2014.

[15] “Series Resonance Circuit,” Electronics Tutorials, 2017. [Online]. Available: http://www.electronics-tutorials.ws/accircuits/series-resonance.html.

[16] J. W. Nilsson and S. A. Riedel, Electric Circuits, 10th ed. Harlow: Pearson Education, 2015.

[17] T. S. V. K. Iyer, Circuit Theory. New Delhi: Tata McGraw-Hill, 2006.

[18] J. D. Irwin and R. M. Nelms, Basic Engineering Circuit Analysis, 11th ed. Hoboken: John Wiley & Sons, 2015.

[19] M. Wang, Understandable Electric Circuits. Stevenage, UK: IET, 2005.

[20] G. Kansal and A. Sharma, "Decreasing Parasitic Capacitance in IC Layouts," EDN Network, 04-Jan-2014. [Online]. Available: https://www.edn.com/design/analog/4426479/Decreasing-parasitic-capacitance-in-IC-layouts.

[21] F. P. Miller and A. F. Vandome, Biot-Savart Law. Alphascript Publishing, 2009.

[22] R. Fitzpatrick, "The Biot-Savart Law," University of Texas Department of Physics, 02-Feb-2006. [Online]. Available: http://farside.ph.utexas.edu/teaching/em/lectures/node38.html.

[23] J. R. Reitz, F. J. Milford, and R. W. Christy, Foundations of Electromagnetic Theory, 4th ed. Noida: Pearson, 2013

[24] S. Hughes, "Lecture 10: Magnetic Force; Magnetic Fields; Ampère's Law," in Massachusetts Institute of Technology Department of Physics, 2005. [Online]. Available: http://web.mit.edu/sahughes/www/8.022/lec10.pdf

[25] R. Fitzpatrick, Classical Electromagnetism: An Intermediate Level Course. The University of Texas at Austin.

[26] L. B. Rees, Faraday's Law of Induction. Brigham Young University, 2006. [Online]. Available: https://www.physics.byu.edu/faculty/rees/220/book/lesson11.pdf

[27] Boundless Physics. LumenCandela. [Online]. Available: https://courses.lumenlearning.com/boundless-physics/

[28] L. C. Shen and J. A. Kong, Applied Electromagnetism, 3rd ed. Boston: PWS Pub. Co., 1995.

[29] D. Fleisch, A Student's Guide to Maxwell's Equations. Cambridge University Press, 2008.

[30] J. Stewart, Calculus: Early Transcendentals, 8th ed. Boston, MA: Cengage Learning, 2015.

[31] S. Deshmukh and H. Huang, "Wireless Interrogation of Passive Antenna Sensors," Measurement Science & Technology, vol. 21, no. 3, Mar. 2010.

[32] C. Cho and X. Yi, "Passive Wireless Frequency Doubling Antenna Sensor for Strain and Crack Sensing," IEEE Sensors Journal, vol. 16, no. 14, Jul. 2016.

[33] J. D. Kraus, Antennas, 2nd ed. New York: McGraw-Hill, 1989.

[34] S. J. Orfanidis, Electromagnetic Waves and Antennas. Rutgers University, 2016.

[35] W. K. H. Panofsky and M. Phillips, Classical Electricity and Magnetism, 2nd ed. Mineola, NY: Dover Publications, 2005.

[36] "NTS," NTS: National Technical Systems. [Online]. Available: https://www.nts.com/locations/pittsfield.

[37] "Pearson Current Monitor Model 4418," Pearson Electronics, Inc. [Online]. Available: http://www.pearsonelectronics.com/pdf/4418.pdf

[38] EMSS, "FEKO Comprehensive Electromagnetic Solutions User's Manual", EM Software & Systems-S.A. (Pty) Ltd. 32 Techno Avenue, Technopark, Stellenbosch, 7600, South Africa, 2011.

[39] L.J. Smith, K.L. Dudley, G.N. Szatkowski, "Computational Electromagnetic Modeling of SansEC Sensors", 27th International Review of Progress in Applied Computational Electromagnetics; (ACES) Williamsburg, VA; 27-31 Mar. 2011.

[40] Z. Chen and M. M. Ney, "Method of Moments: A General Framework for Frequency- and Time-domain Numerical Methods," 2007 Workshop on Computational Electromagnetics in Time-Domain, 2007.

[41] Z. Chen and M. M. Ney, "The Method of Weighted Residuals: A General Approach to Deriving Time – and Frequency-Domain Numerical Methods," IEEE Antennas and Propagation Magazine, vol. 51, no. 1, pp. 51–70, 2009.

[42] "DADiSP® Product Family and Services," DSP Development Corporation: DADiSP Product Family. [Online]. Available: http://www.dadisp.com/products.htm.

[43] J. P. Brainard and R. A. Anderson, "Flashover of Resistor and Varistor Materials," IEEE Xplore, Oct-2016. [Online]. Available: http://ieeexplore.ieee.org/document/7683874/

[44] F. Mahmood and M. Lehtonen, "Experimental Investigation of Lightning Initiated Flashover Faults in MV Lines," 2014 ICHVE International Conference on High Voltage Engineering and Application, 2014.

[45] "Image Processing Toolbox," The MathWorks, Inc. [Online]. Available: https://www.mathworks.com/products/image.html

[46] E. A. Silva and K. Panetta, "Quantifying Image Similarity using Measure of Enhancement by Entropy," CiteSeerX, May-2007. [Online]. Available: http://citeseerx.ist.psu.edu/viewdoc/download?doi=10.1.1.160.6126&rep=rep1&type=pdf

[47] A. F. Hassan and D. Cailin, “An Information-theoretic Image Quality Measure: Comparison with Statistical Similarity,” Journal of Computer Science, 2014. [Online]. Available: http://ro.ecu.edu.au/ecuworkspost2013/221/

[48] “MATLAB,” The MathWorks, Inc. [Online]. Available: https://www.mathworks.com/products/matlab.html?s_tid=hp_products_matlab

[49] “Disclaimers, Copyright Notice, and Terms and Conditions of Use - NASA Scientific and Technical Information (STI) Program,” NASA STI | Scientific and Technical Information Program, 24-Oct-2012. [Online]. Available: https://www.sti.nasa.gov/disclaimers/#.WeO4kVtSyUl. [Accessed: 15-Oct-2017].

APPENDIX

A. PERMISSIONS

Disclaimers, Copyright Notice, and Terms and Conditions of Use

DISCLAIMERS

Disclaimer of Liability: With respect to materials (e.g., documents, photographs, audio recordings, video recordings, tools, data products, or services) on or available through download from this Web site, neither the U.S. Government, NASA, nor any of its employees or contractors make any representations or warranties, express, implied, or statutory, as to the validity, accuracy, completeness, or fitness for a particular purpose; nor represent that use would not infringe privately owned rights; nor assume any liability resulting from the use of such materials and shall in no way be liable for any costs, expenses, claims, or demands arising out of the use of such materials.

Disclaimer of Endorsement: Neither the U.S. Government nor NASA endorse or recommend any commercial products, processes, or services. Reference to or appearance of any specific commercial products, processes, or services by trade name, trademark, manufacturer, or otherwise, in NASA materials does not constitute or imply its endorsement, recommendation, or favoring by the U.S. Government or NASA. The views and opinions of authors expressed on NASA Web sites or in materials available through download from this site do not necessarily state or reflect those of the U.S. Government or NASA, and they may not be used for advertising or product endorsement purposes.

COPYRIGHT NOTICE

General
Generally, United States government works (works prepared by officers and employees of the U.S. Government as part of their official duties) are not protected by copyright in the U.S. (17 U.S.C. §105) and may be used without obtaining permission from NASA. However, U.S. government works may contain privately created, copyrighted works (e.g., quote, photograph, chart, drawing, etc.) used under license or with permission of the copyright owner. Incorporation in a U.S. government work does not place the private work in the public domain.

Moreover, not all materials on or available through download from this Web site are U.S. government works. Some materials available from this Web site may be protected by copyrights owned by private individuals or organizations and may be subject to restrictions on use. For example, contractors and grantees are not considered Government employees; generally, they hold copyright to works they produce for the Government. Other materials may be the result of joint authorship due to collaboration between a Government employee and a private individual wherein the private individual will hold a copyright to the work jointly with U.S. Government. The Government is granted a worldwide license to use, modify, reproduce, release, perform, display, or disclose these works by or on behalf of the Government.

While NASA may publicly release copyrighted works in which it has government purpose licenses or specific permission to release, such licenses or permission do not necessarily transfer to others. Thus, such works are still protected by

copyright, and recipients of the works must comply with the copyright law (Title 17 United States Code). Such copyrighted works may not be modified, reproduced, or redistributed without permission of the copyright owner.

If a recognizable person appears in a photograph or video recording, or the talent (such as a performance or narration) of a known individual is included in an audio or video recording, use for commercial purposes may infringe on a right of privacy or publicity. Permission should be obtained from the recognizable person or known individual. However, if the intended use of NASA material is primarily for educational or informational purposes (e.g., books, newspapers, and magazines reporting facts of historical significance), then such uses will generally not be considered an infringement of such personal rights.

Additional copyright information concerning copyright status is given in the metadata for the documents and other STI.

Documents

Documents available from this Web site are not protected by copyright unless noted. If not copyrighted, documents may be reproduced and distributed, without further permission from NASA. However, some documents or portions of documents available from this site may have been contributed by private individuals or organizations and may be copyrighted. If copyrighted, permission should be obtained from the copyright owner prior to use (e.g., modification, reproduction, or redistribution).

Photography

Photographs available from this Web site are not protected by copyright unless noted. If not copyrighted, photographs may be reproduced and distributed without further permission from NASA. If copyrighted, permission should be obtained from the copyright owner prior to use. If a recognizable person appears in a photograph, use for commercial purposes may infringe a right of privacy or publicity and permission should be obtained from the recognizable person.

Audio Recordings

Audiotape recordings available from this Web site are not protected by copyright unless noted. If not copyrighted, audio recordings may be excerpted or reproduced and distributed, without further permission from NASA. If copyrighted, permission should be obtained from the copyright owner prior to use. Use for a commercial purpose of a portion or segment of an audio recording that incorporates the talent (such as narration or music) of a known individual, may infringe a right of publicity and permission should be obtained from the known individual.

Video Recordings

Video recordings (videotape and motion picture recordings) available from this Web site, including audio recordings therein, are not protected by copyright unless noted. If not copyrighted, video recordings may be reproduced and distributed, without further permission from NASA. If a video recording is copyrighted in its entirety or a portion of a recording contains copyrighted material, such as music or video footage, permission should be obtained from the copyright owner prior to use. Use for a commercial purpose of any portion or segment of a video recording that displays a recognizable person, or the talent (such as a performance or narration) of a known individual, may infringe on a right of privacy or publicity, and permission should be obtained from the recognizable person or known individual.

TERMS AND CONDITIONS OF USE

Unless additional terms and conditions are provided with specific materials, the following information specifies the terms and conditions under which the materials on or available from this Web site may be used.

- NASA does not grant exclusive use rights with respect to NASA material.

- NASA should be acknowledged as the source of its material.
- It is unlawful to falsely claim copyright or other rights in NASA material.
- Material available from this Web site may include visible NASA identifiers (NASA name and initials, NASA Insignia, NASA Logotype, NASA Seal, and NASA Program Identifiers). Use of such material is generally non-objectionable, provided the NASA identifiers appear in their factual context. Other uses of the NASA Insignia, Seal, Logotype, or Program Identifiers require approval under 14 C.F.R. Part 1221. Use of the NASA name and initials is protected under 42 U.S.C. 2459b.
- NASA material may not be used to state or imply the endorsement by NASA or by any NASA employee of commercial products, processes, or services, or used in any other manner that might mislead.
- Use of NASA identifiers which would express or imply such an endorsement is strictly prohibited.
- Use of the NASA name or initials as an identifying symbol by organizations other than NASA is strictly prohibited.
- NASA does not indemnify nor hold harmless users of NASA material, nor release such users from copyright infringement.
- NASA personnel are not authorized to sign indemnity or hold harmless statements, releases from copyright infringement, or documents granting exclusive use rights.

VITA

Kayla Farrow

Department of Electrical and Computer Engineering

Old Dominion University

Norfolk, VA, 23529

(202)-630-9009

kfarr017@odu.edu

Education:

Kayla Farrow received a Bachelor of Science degree in Electrical Engineering from Old Dominion University in 2015.

Professional Associations:

Institute of Electrical and Electronics Engineers (IEEE)

National Society of Black Engineers (NSBE)

Society of Women Engineers (SWE)